PHYSICAL REVIEW C VOLUME 35, NUMBER 5 MAY 1987

Fragment production in intermediate energy heavy ion reactions

B. V. Jacak,* G. D. Westfall, G. M. Crawley, D. Fox, C. K. Gelbke, L. H. Harwood,
B. E. Hasselquist,† W. G. Lynch, D. K. Scott, H. Stöcker,‡
M. B. Tsang, and G. Buchwald‡
National Superconducting Cyclotron Laboratory, Michigan State University, East Lansing, Michigan 48824

T. J. M. Symons
Nuclear Science Division, Lawrence Berkeley Laboratory, Berkeley, California 94720
(Received 28 August 1986)

The emission of intermediate rapidity fragments with $A \leqq 14$ has been studied in 42 to 151 MeV/nucleon Ar- and Ne-induced reactions on Al, Ca, and Au targets. The energy spectra were fitted assuming emission from a single source moving with a velocity intermediate between that of the projectile and target. The extracted temperatures were independent of fragment mass, indicating that the fragments had a common source. The spectra for fragments as heavy as nitrogen were also well described using the coalescence model and the resulting coalescence radii were independent of fragment mass. The observed fragment production cross sections were fitted with a quantum statistical model from which the entropy produced was extracted. This entropy was found to be much less than that derived from d/p ratios and higher than the entropy displayed by target-like fragments. The light particle spectra were compared to a model utilizing a solution of the Boltzmann equation incorporating mean field and Pauli blocking effects to describe the proton spectra from Ar + Ca. Nuclear fluid dynamics calculations agreed reasonably well with the higher energy data but could not describe the 42 MeV/nucleon data.

I. INTRODUCTION

High energy nucleus-nucleus collisions provide a unique tool for studying nuclear matter at excitations and densities far from the normal ground state.[1-4] The study of inclusive light particle (n, p, d, t, ^{3}He and ^{4}He) (Refs. 5–20) and complex fragment (Li–Ne) (Refs. 5, 21, and 22) spectra has produced a great deal of information concerning the geometry and basic interaction mechanisms that describe these reactions. Of special interest are reactions induced by nuclei with energies from 10 to 200 MeV/nucleon, where the reaction mechanisms are thought to change from mean field phenomena at low energies to localized interaction regions where single nucleon-nucleon scatterings become important at higher energies. Several very different theoretical frameworks have been devised to describe the low energy and the high energy regimes, but a complete description of the transition from low to high energy does not yet exist. In this paper we present a survey of inclusive measurements covering this transition regime ranging from 42 to 151 MeV/nucleon incident energy, where the velocity of the projectile nuclei range from the Fermi velocity up to half the speed of light.

An important concept in these reactions is the separation of the observed fragments into participants and spectators. Because the relative velocity of the nuclei is higher than the speed of sound in nuclear matter, reactions between two high energy nuclei are localized to the overlapping volume of the nuclei, while the remaining volume of the target and projectile nuclei retain much of their original velocity and are only slightly excited. Fragments from the projectile spectators are observed predominately at forward angles near beam velocity, while those from the target spectators are emitted almost isotropically in the laboratory at energies characterized by the Coulomb barrier. Participant particles, on the other hand, are emitted at all angles and at energies up to several times the incident energy per nucleon. Thus one may select kinematically those fragments emitted from the interaction zone by studying energy spectra at large angles and high energies. This interaction zone has been termed a nuclear fireball [5,23] and can be characterized as a source of particles moving in the laboratory with a velocity intermediate between those of the projectile and target nuclei. By systematically varying the incident energy, the projectile, and the target, one can study the properties of nuclear matter far from the normal ground state.

Light particle spectra from light projectile-induced reactions on heavy targets have been fitted assuming emission from a thermalized subset of target and projectile nucleons, a method which resulted in a successful parametrization of light particle data at incident energies as low as 10 MeV/nucleon and as high as 2.1 GeV/nucleon.[13,14] The parameters describing the spectra, the production cross section, the temperature, and the velocity of the moving source, vary smoothly with bombarding energy.[14] This smoothness is somewhat surprising because a 10 MeV/nucleon projectile moves slowly enough to allow considerable exchange of information with the target. It has been suggested that at bombarding energies where the participants and spectators are not yet well separated, a local thermalized zone, or hot spot, is formed.[1,24-26] As the bombarding energy goes up, this hot spot breaks away from the target and becomes the participant zone or fireball.

In order to gain more detailed information about the reaction mechanisms, experiments with some kinematic restrictions have been performed. Many of these first coincidence experiments have focused on coincidences between large fragments arising from projectile or target remnants and fast charged particles. Studies at and below 35 MeV/nucleon have revealed that light charged particles associated with a projectile remnant are most likely to be found in one of two places. The first place is focussed directly behind the fragment, consistent with a sequential breakup of the excited projectile.[27–30] The second is focused to the opposite side of the beam from the projectile fragment, suggesting emission from a recoiling source.[31–33]

The observation that many gross features change very slowly and regularly between 20 and 200 MeV/nucleon has inspired the use of theories at the limits of their applicability. The expected transition from the long mean free path of nucleons to the region where two-body collisions are important has led to the application of time-dependent Hartree-Fock (TDHF) and hydrodynamical calculations at intermediate energies.[34] These two approaches are compared for a central collision in Fig. 1. The density plots on the left show the time evolution of a Kr + Kr reaction in a TDHF calculation. It is clear that the nuclei pass through one another and very little compression takes place. The hydrodynamical calculation shown in the right hand side of Fig. 1 indicates a total lack of transparency of the nuclei. The incoming matter is stopped and squeezed out to the side. Realistically, one would expect a mixture of the one-body dissipation inherent in TDHF and the two-body dissipation of hydrodynamics at intermediate energies.[35]

A theory aimed at these reactions must include the nuclear mean field, Pauli blocking, and nucleon-nucleon collisions. A convenient framework for such a theory is the Monte Carlo method used in intranuclear cascade calculations.[36–42] Most cascade calculations include only two-body collisions with a simple approximation for the Pauli principle which makes them ineffective for intermediate energy collisions. First attempts to fully incorporate the required physics use a Monte Carlo solution of the full

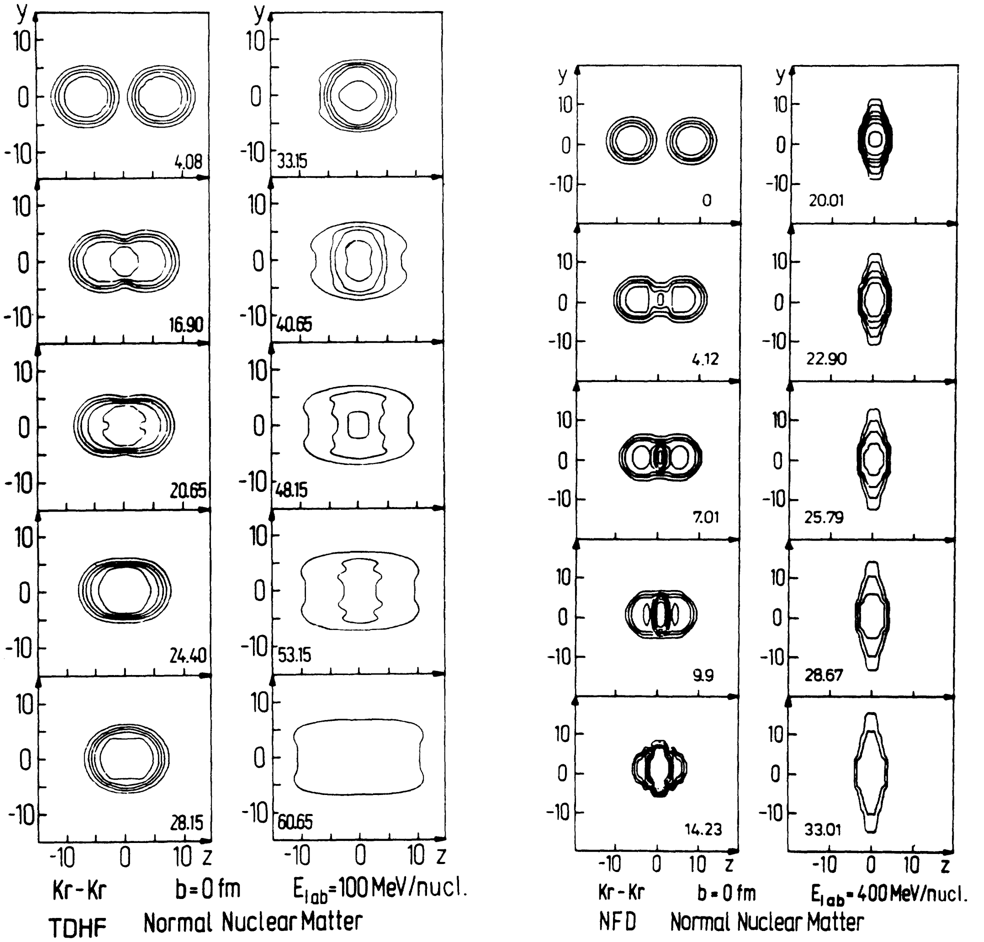

FIG. 1. Density contour plots exhibiting the reaction dynamics predicted by TDHF (left) and a nuclear fluid dynamical model (right).

Boltzmann equation.[43,44] This method agrees well with high energy data[45] and shows promising results at intermediate energies.[20] Inclusive proton cross sections for 40—140 MeV/nucleon reactions, where 80—90% of the two nucleon collisions are Pauli blocked, are well reproduced.

In this work we present single particle inclusive measurements of particles with $1 \leqq A \leqq 14$ from 42, 92, and 137 MeV/nucleon Ar + Au and Ar + Ca reactions. Also, we report light particle ($1 \leqq A \leqq 4$) measurements from 100 and 156 MeV/nucleon Ne + Au and 156 MeV/nucleon Ne + Al. The details of experimental setup, detector calibration techniques, data acquisition and data reduction are presented in Sec. II.

The double differential spectra look approximately exponential as a function of the energy of the observed particle. They are presented in Sec. III along with contours of constant cross section plotted in the plane of rapidity versus perpendicular momentum/mass. These plots point to the existence of a source intermediate in rapidity between the projectile and the target.

In Sec. IV the spectra are parametrized via a single moving source prescription. The source temperature and velocity and the integrated cross section for particle emission are determined via a least squares fit to the measured spectra of a relativistic Boltzmann distribution in a moving frame. The systematics of the source parameters are examined as a function of the projectile, target, and beam energy.

Section V reviews several models of the reaction which incorporate thermalization of the incident energy. The light particle spectra are used to explore the low energy limits of applicability of the fireball model.[23] The assumption of thermal and chemical equilibrium is used to extract information about bulk properties of nuclear matter from the inclusive data. If the heated subsystem freezes into various fragments, the relative yields of the fragments reflect the entropy in the system at the time of freezeout.[22,47] Alternatively, the fragments may be formed by coalescence of nucleons close together in phase space.[46] The fragment spectra are compared to proton spectra to investigate the validity and extent of this phenomenon.

In Sec. VI, two dynamical models are discussed. The present data are used as a first test of the Boltzmann equation approach to intermediate energy heavy ion collision.[20,43] The dynamics of the Ar + Ca interaction are followed using a Monte Carlo solution of the equation.[43] This model incorporates the Pauli blocking and nuclear mean field necessary for low energy reactions and the nucleon-nucleon collision terms typical of high energy approaches, and is applied at all three bombarding energies. The light particle data are also used to test the performance of hydrodynamical[47,48] models in this energy regime.

The last section summarizes the experiments and calculations presented in this work which show that the transition between low and high energy nuclear reactions is a smooth one and that intermediate energy collisions show characteristics of both. Single particle inclusive measurements provide a useful survey, but coincidence experiments with kinematic selection of the measured quantities are required to trace the evolution of specific reaction mechanisms.

II. EXPERIMENTAL

The experiments were done at the Lawrence Berkeley Laboratory (LBL) Bevalac.

A. Ar-induced reactions

The experimental setup consisted of three particle telescopes. One telescope consisted of two silicon ΔE detectors and a NaI E detector to detect particles of $Z=1,2$. This telescope was mounted on a movable arm inside the LBL Low Energy Beam Line 1.5 m scattering chamber and was moved from 30° to 130°. Mounted on a separately movable arm in the scattering chamber were two stacks of silicon detectors for measurement of particles with $Z=3-7$. The scattering chamber arrangement is shown in Fig. 2. All three telescopes achieved isotopic resolution for the elements detected. The data were stored on magnetic tape in event-by-event mode and analyzed off line.

The targets used were self-supporting and consisted of 80 mg/cm^2 Au and 35 mg/cm^2 Ca for the 42 and 92 MeV/nucleon Ar beams, and 200 mg/cm^2 Au and 160 mg/cm^2 Ca for the 137 MeV/nucleon Ar beam.

The normalizations were determined by the integrated beam current in an ionization chamber downstream from the scattering chamber. The chamber was calibrated by

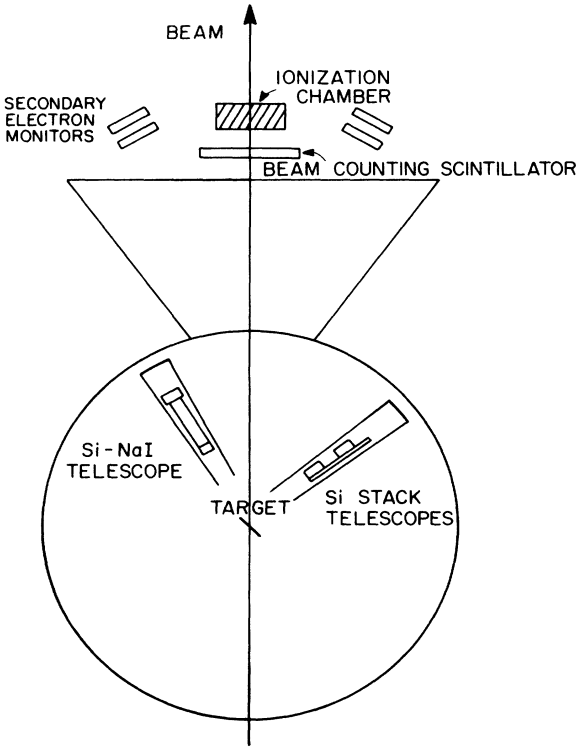

FIG. 2. Scattering chamber configuration for measurement of the Ar-induced reactions.

lowering the beam intensity such that individual beam particles could be counted in a plastic scintillator directly in front of the ionization chamber, as shown in Fig. 2. The absolute normalizations were accurate to within 20%. In the case of the 42 MeV/nucleon beam, however, the beam monitoring did not function properly and the resulting absolute normalizations are only known to within a factor of 3. This method was compared to the rate of secondary particle production as the beam traversed the target, measured by pairs of plastic scintillators on either side of the ionization chamber. The procedures agreed to within 5%. The secondary particle scintillators were also used to monitor the beam centering on the target. The ratio of secondary particles on the left and right side of the chamber exit was calculated for each beam pulse, and data from pulses differing greatly from the average were rejected during the off-line analysis. Several percent of the beam pulses were rejected this way.

1. *Detector systems*

a. Si-NaI telescope. Light particles (p, d, t, ^{3}He, ^{4}He and ^{6}He) were measured with a ΔE-E telescope consisting of two silicon ΔE detectors, 400 μm and 5 mm in thickness, backed by a 10 cm NaI E detector. Light particles from 15 to 160 MeV/nucleon were stopped. This telescope subtended 7.2 msr, and was used to measure spectra from 30° to 130° in 20° steps. Events were accepted by detection of a signal in the second silicon detector.

The energy calibration for the silicon detectors was done by injecting a known amount of charge by means of a chopper pulser in the input stage of the detector preamplifiers and using the measured values of the ionization energy of silicon, $\epsilon = 3.67$ eV/ion pair.[49] The NaI detector was calibrated with direct beams of protons and ^{4}He at 150 MeV/nucleon, and with these beams degraded to 143, 125, 103, 81, 58, and 35 MeV/nucleon. The energy resolution was approximately 5%. The energy spectra were corrected for the energy loss in half the target thickness and for the reaction losses of particles in the detectors.

The fraction of reaction loss for protons as a function of proton energy was taken from Ref. 50. The proton cross sections were scaled for different fragments using Eq. (1) with Z_1, A_1 being the atomic number and mass number of the observed fragment and Z_2, A_2 being the effective atomic number and mass number of the stopping medium. These data were fitted with the equation

$$\sigma_R = N\pi r^2(1 - V_c/E)[1 + (\kappa/E)^{1.2}] , \tag{1}$$

where E is the energy of the stopping particle, N is a normalization constant, and $r = 1.2(A_1^{1/3} + A_2^{1/3} - 1)$ fm $V_c = 1.44(Z_1 Z_2/r)$ MeV, and $\kappa = 20$ MeV. N was taken to be 1.1 for Si and 2.0 for NaI. The value of κ determines the energy at the peak of the cross section. In order to make the correction, the detector was divided up into slices, and the particle energy in each slice was calculated from the entrance energy using range-energy tables. The reaction cross section for each slice was then calculated from Eq. (1) and the reaction probability f of a particle was given by integration over the slices

$$f = 1 - \exp\left[-\sum_i n_i \sigma_i \right] , \tag{2}$$

where n_i is the number of atoms/cm^2 in cell i and σ_i is the average reaction cross section in cell i. This reaction probability was calculated for each energy bin in the spectrum of each particle, and the cross section corrected by the factor $1/(1-f)$. The corrections were approximately 3% for 50 MeV protons, 9% for 100 MeV protons, and 18% for 150 MeV protons.

b. Multi-Si telescopes. For the heavy fragments, from lithium to nitrogen, the detection system consisted of two stacks of silicon detectors. A low energy stack consisted of three detectors of thickness 100 μm, 300 μm, and 5.0 mm. The high energy stack was comprised of five detectors, two 800 μm counters, and three counters 5.0 mm in thickness. The range of detected fragments in these two telescopes is given in Table I. The telescopes subtended 14.0 and 16.0 msr, with opening angles of 7.6° and 8.2°, respectively. Both telescopes were mounted at the same scattering angle, 10° out of plane, and were rotated together to measure spectra from 30° to 130° in 20° steps. Events in either telescope were accepted upon detection of a signal in the second detector of the stack.

These telescopes were calibrated with the same pulser system as the silicon detectors in the light particle telescope. In addition, they were calibrated with a direct beam of ^{20}Ne at 150 MeV/nucleon, and degraded to 137, 115, 93, 68, and 40 MeV/nucleon. The resulting energy calibration was good to 5%. The energy spectra were corrected for the energy loss in half the target thickness. The energy spectra were combined, with the cross sections in the region of overlap of the two telescopes averaged together, weighted by the statistical error.

2. *Electronics*

The three telescopes were operated in a parallel fashion with each telescope having its own dead-time circuit, CAMAC bit register, and CAMAC analog-to-digital converter (ADC). Pile-up rejection circuitry (PUR), with a pulse pair resolution of ≤ 100 nsec, was used to set a bit in the telescope-dedicated bit register for a good event. Each telescope produced its own ADC gate and interrupt for the CAMAC branch driver of the PDP 11/34 computer.

TABLE I. Energy range in MeV of fragments detected in the multielement silicon telescopes used for the Ar-induced reactions.

Fragment	Thin Si Stack	Thick Si Stack
^{6}Li	23–240	80–445
^{7}Li	24–256	85–480
^{8}Li	26–275	92–510
^{9}Li	27–288	96–540
^{7}Be	34–368	123–689
^{9}Be	38–407	136–762
^{10}Be	40–424	142–795
^{10}B	52–554	185–900
^{11}B	54–575	192–1000
^{12}C	66–708	236–1320

The live time was monitored by scaling the number of times each telescope received a valid event and the number of valid events.

3. Data reduction

Particle identification was achieved by placing gates on the ΔE-E two dimensional histograms. Double differential spectra were generated by collecting the events into 5 MeV/nucleon bins for light fragments and 15 MeV bins for heavy fragments. The cross sections were generated using the normalizations described above and correcting for the telescope solid angle and dead time.

B. Ne-induced reactions

The scattering chamber arrangement for the Ne-induced reactions is shown in Fig. 3. Aluminum fans were mounted on the two movable arms, and several telescopes were mounted on each fan. The light particles were detected with seven ΔE-E telescopes.

Two energies of ^{20}Ne were used, 156 and 100 MeV/nucleon. The 156 MeV/nucleon beam was used to bombard a 100 mg/cm^2 Au target and a 103 mg/cm^2 Al target. Measurements with the 100 MeV/nucleon beam were done for the Au target only.

The relative normalizations and beam centering monitors were done in the same manner as described above, and the normalizations and energy calibrations checked by comparing the overlapping spectra. The relative normalizations agreed to within 5%, while the energy calibrations for the various types of detectors were good to about 10%. The absolute normalizations were obtained with the ionization chamber, as above, and were accurate to within 25%.

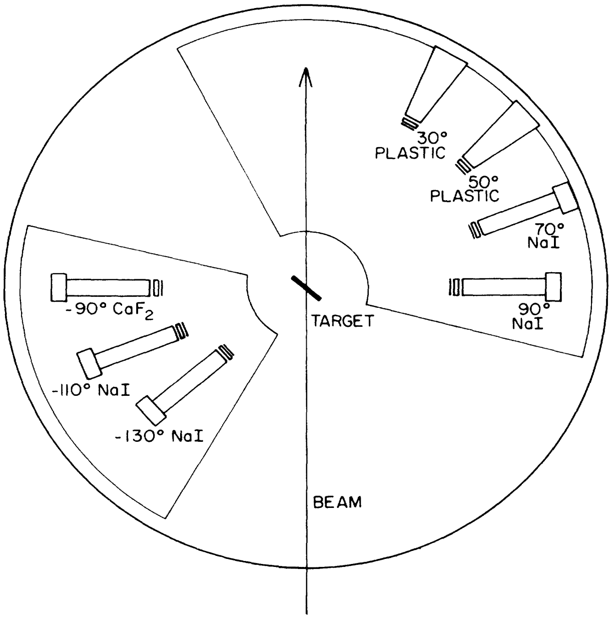

FIG. 3. Scattering chamber configuration for measurement of the Ne-induced reactions.

1. Detector systems

The seven light particle telescopes were arranged to measure spectra at six angles with respect to the beam direction. Each telescope had two silicon ΔE detectors, 400 μm and 5 mm thick, except at 50°, where the first detector was 800 μm. All silicon detectors were calibrated with the pulser system described above. The stopping detectors were of three different types: plastic scintillator detectors at 50°, NaI at 90°, 110°, and 130°, and CaF$_2$ at 90°. The arms were moved during the experiment by 20° in order to allow overlap spectra among the different types of detectors. A summary of the telescopes, opening angles, and solid angles is given in Table II.

The stopping detectors in the light particle telescopes were calibrated with direct beams of protons at 150, 90, and 50 MeV, and with a 150 MeV/nucleon ^{4}He beam. The calibrations yielded overlap spectra among different types of detectors which agreed to within 10%. The light particle spectra were corrected for reaction losses using the method described above.

2. Electronics

The seven telescopes were operated in parallel. The triggers from the telescopes forward of 70° were scaled down a factor of 10. The pulse height from each detector was recorded via a CAMAC ADC, and each telescope with a valid event set a bit in a CAMAC bit register. A strobe to the branch driver was issued whenever a valid event in $\Delta E2$ of one telescope was accompanied by a signal in the $\Delta E1$ or E detector.

3. Data reduction

The particle identification was done by determining which detector the particle stopped in and calculating the function[51]

$$\mathscr{P} = (\Delta E + E)^j - (E)^j \,, \tag{3}$$

using the stopping detector to determine E, and the detector before it for ΔE. The exponent j was varied to linearize the $\mathscr{P}$ values as a function of energy for each particle type. The value of j was typically between 1.5 and 2.0. Reaction loss corrections were applied as described above. The cross sections were corrected for the telescope solid angle, scale-down factor, and system dead time.

III. RESULTS

A. Double differential cross sections

Figures 4–7 show the double differential cross sections of hydrogen and helium isotopes produced in Ar + Au and Ar + Ca at 137, 92, and 42 MeV/nucleon. They were measured at 30°, 50°, 70°, 90°, 110°, and 130° in the laboratory, with each angle represented by a different symbol. The error bars show statistical errors only. The points in the spectra of Figs. 4–7 in the region of 20–30 MeV/nucleon are suppressed because of nonlinearities resulting from small dead layers in the silicon detectors and the entrance window into the NaI crystal.

TABLE II. Composition, size, highest energy proton stopped, and opening and solid angles for light particle telescopes used for the Ne-induced reactions.

Lab angle (deg)	Si ΔE (mm)	E (cm)	Max. p energy (MeV)	Angle (deg)	Solid angle (msr)
30	0.8, 5	20.0 plas.	176	8.2	16.1
50	0.8, 5	20.0 plas.	176	8.3	16.4
70	0.4, 5	7.5 NaI	158	5.3	6.9
90	0.4, 5	5.0 CaF_2	138	5.4	6.9
90	0.4, 5	10.0 NaI	168	3.9	3.6
110	0.4, 5	5.0 NaI	126	4.6	5.0
130	0.4, 5	5.0 NaI	126	6.7	10.7

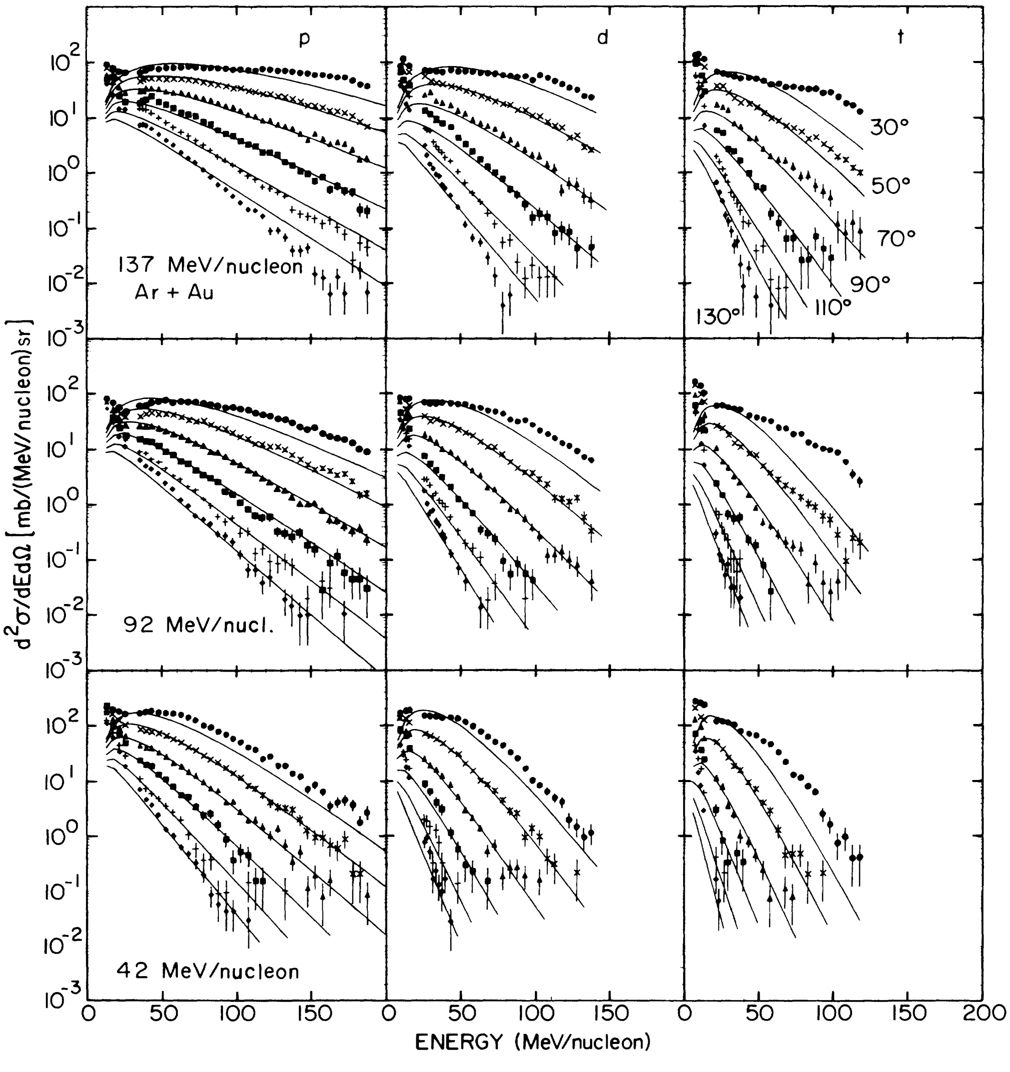

FIG. 4. Double differential cross sections for hydrogen isotopes produced in Ar + Au reactions at 137, 92, and 42 MeV/nucleon. Data at 30°, 50°, 70°, 90°, 110°, and 130° are shown for each particle. The solid lines are fits with a single moving source parametrization.

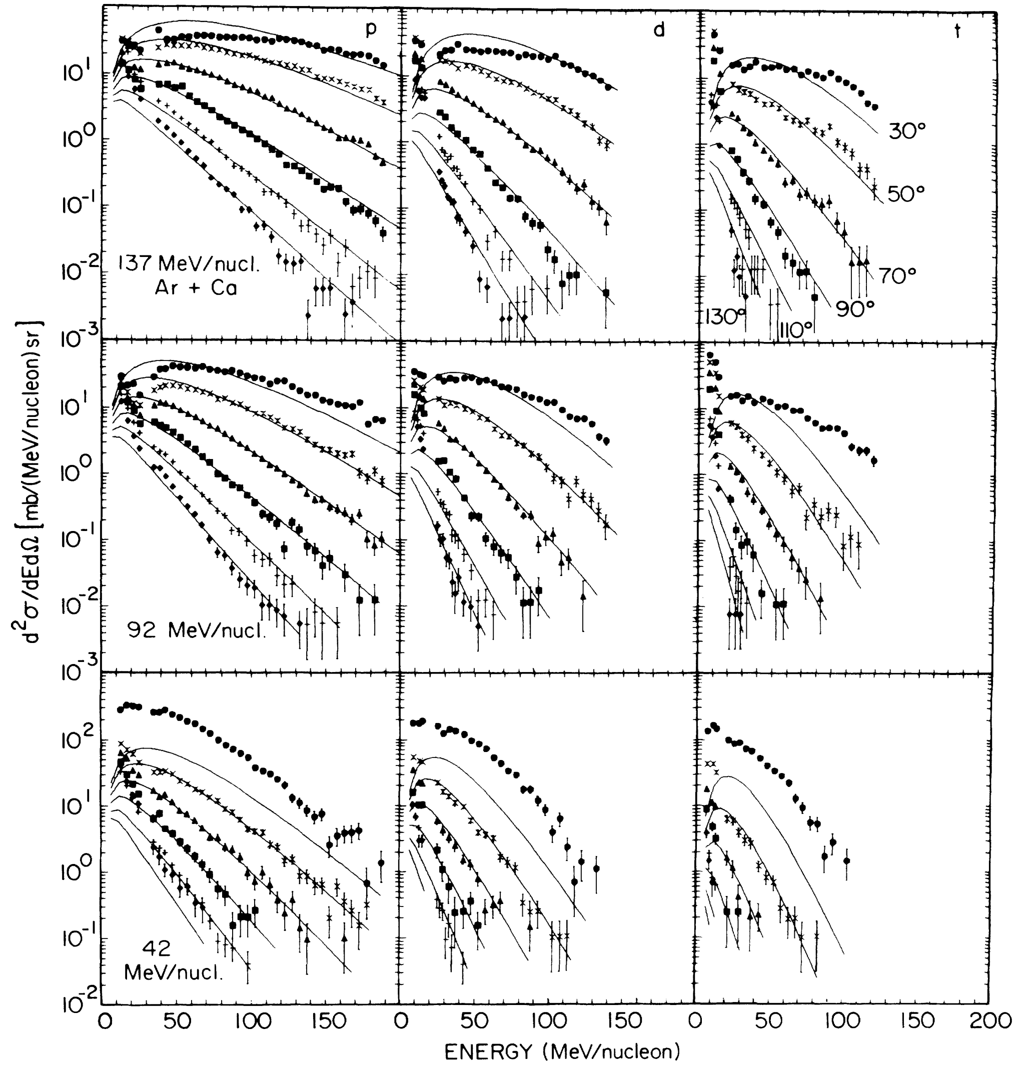

FIG. 5. Double differential cross sections for hydrogen isotopes produced in Ar + Ca reactions.

Above 35 MeV/nucleon, the energy spectra decay approximately exponentially with increasing energy. For larger angles the cross sections decrease by several orders of magnitude as a function of energy. A distinct low energy component of quite different slope is visible below 25 MeV/nucleon whose angular distribution is much less forward peaked than the higher energy component.

The high energy tails become steeper for heavier particles, and much steeper as the bombarding energy is decreased. The maximum in the double differential cross section does not change rapidly as one goes from 137 to 92 MeV/nucleon bombarding energy. The general features of the low energy part of the spectra, including the slope, do not change significantly with bombarding energy.

Light particles are produced with smaller cross sections in Ar + Ca reactions, with somewhat steeper energy spectra than in Ar + Au reactions at the same bombarding energies. At 42 MeV/nucleon particle emission to 30° is enhanced, possibly due to emission from an excited projectile fragment. This effect is more visible in data from the Ca target because there are fewer nucleons participating in the reaction, and the projectile contribution has a greater effect on the observed spectra. At the higher bombarding energies the projectile fragment moves with a larger velocity and the emitted particles are kinematically focused to smaller angles.

Measurements of heavier fragments are reported for 30°, 50°, 70°, and 90°. Results for Li (Figs. 8 and 9), Be (Figs. 10 and 11), and B (Fig. 12) isotopes are shown for all the beam-target combinations. The energy spectra are shown in MeV, rather than MeV/nucleon. The error bars depict statistical errors and errors which arise from joining spectra measured by thin and thick silicon telescopes.

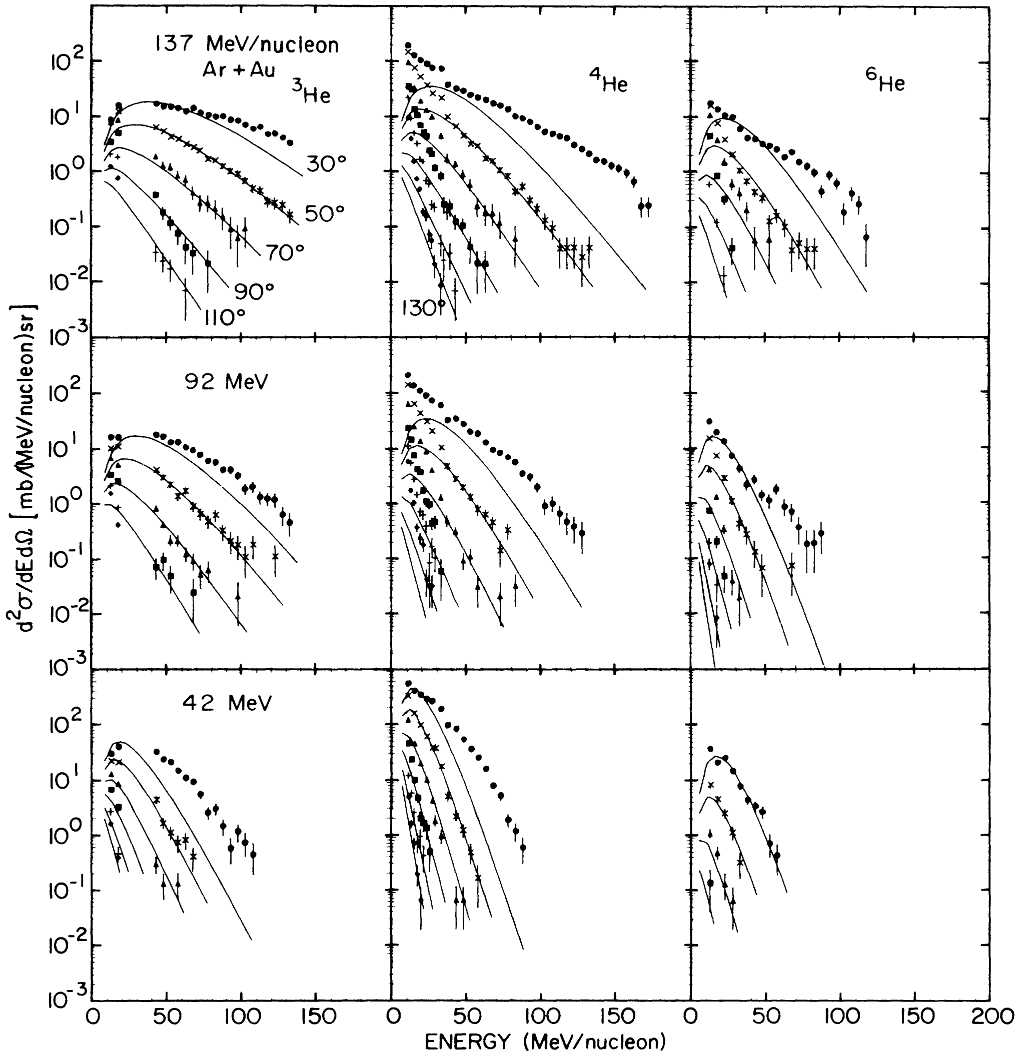

FIG. 6. Double differential cross sections for helium isotopes produced in Ar + Au reactions.

Figure 13 shows the isotope-integrated double differential cross sections for C and N fragments from Ar + Au. Isotope-integrated spectra for B and C fragments from Ar + Ca are given in Fig. 14. At all three bombarding energies, the cross sections for these fragments are considerably lower for Ar + Ca than for Ar + Au reactions.

The energy spectra for the heavier fragments show high energy tails which decay exponentially with increasing energy, similar to the light particle spectra. The slopes of these spectra also get steeper as the bombarding energy is decreased. The heavy fragments, however, differ from the light particles in the behavior of the energy spectra at 30° for fragments with $E > 43$ MeV/nucleon. The 30° spectra are much flatter than the spectra at more backward angles. This is observed for both the Au and Ca target, and for all three bombarding energies.

Figures 15 and 16 show the double differential cross sections of light particles produced in Ne + Au at 156 and 100 MeV/nucleon and in 156 MeV/nucleon Ne + Al, respectively, measured at 50°, 70°, 90°, 110°, and 130° in the laboratory. The general features of the light particle spectra are the same for both projectiles.

B. Rapidity plots

The distribution of longitudinal motion can be analyzed in terms of the rapidity variable

$$y = \tfrac{1}{2}\ln[(E + p_{\parallel})/(E - p_{\parallel})] , \qquad (4)$$

where E and $p_{\parallel}$ are the total energy and longitudinal momentum of a particle. Contours of constant relativistically invariant cross section, $(1/p)d^2\sigma/dE\,d\Omega$, may be plotted in the plane of rapidity versus the transverse momentum, p_t, divided by the mass, m, of the particle.

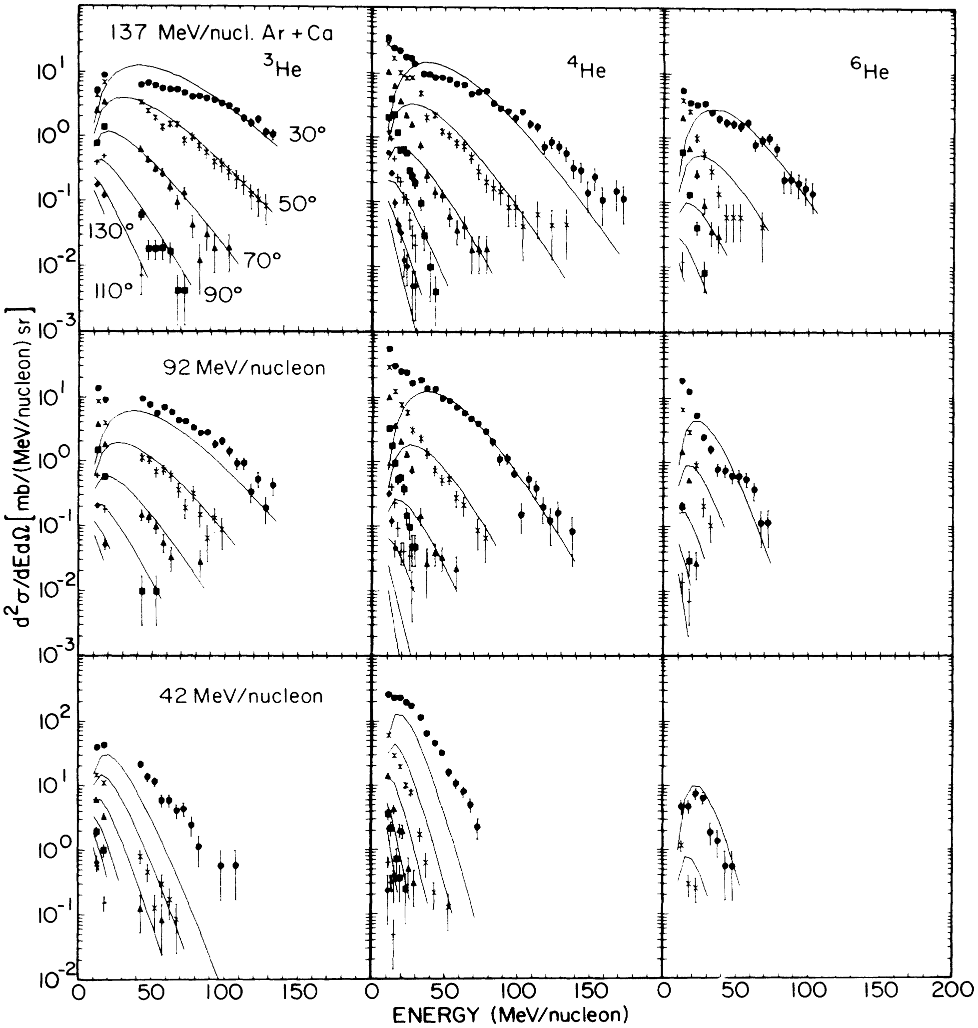

FIG. 7. Double differential cross sections for helium isotopes produced in Ar + Ca reactions.

In such a contour plot, fragments emitted isotropically from a single source will give contour lines centered around the rapidity of the source. These contours are circles in the nonrelativistic limit. When the plot is drawn in the laboratory reference frame, the circles are simply shifted by the rapidity of the emitting source because y is a scalar under Lorentz transformations.

Figure 17 shows rapidity plots in the laboratory frame for protons produced in the Ar-induced reactions for all beam energy—target combinations. The solid curves show the constant cross section contours in y and p_t/m. There are three logarithmically spaced contours in each decade of invariant cross section. The projectile and target rapidities are indicated in the figure by arrows. The dashed circle centered about $y=0$ on each plot shows a contour expected for protons emitted from the target remnant. The contours of observed proton cross section are somewhat elongated, indicating contribution from more than one source. Comparison of the proton contours with the dashed circles suggests that some protons are emitted from a target-like source. The low cross section contours (corresponding to the high energy tails of the spectra greater than 35 MeV) are nearly circular about a rapidity intermediate between the projectile and target rapidities. The arrow labeled y_s indicates the rapidity of a single source best describing the observed high energy proton distribution. The dot-dashed circle represents a sample contour of protons emitted isotropically from this intermediate source. The outer contours approach this circle, suggesting that one may describe the observed proton spectra by emission from two sources: one target-like source and one intermediate rapidity source.

The contours look quite similar for the two targets even though the magnitudes of the cross sections are different. The contours span a smaller region along the rapidity axis as the bombarding energy is lowered, causing the particle

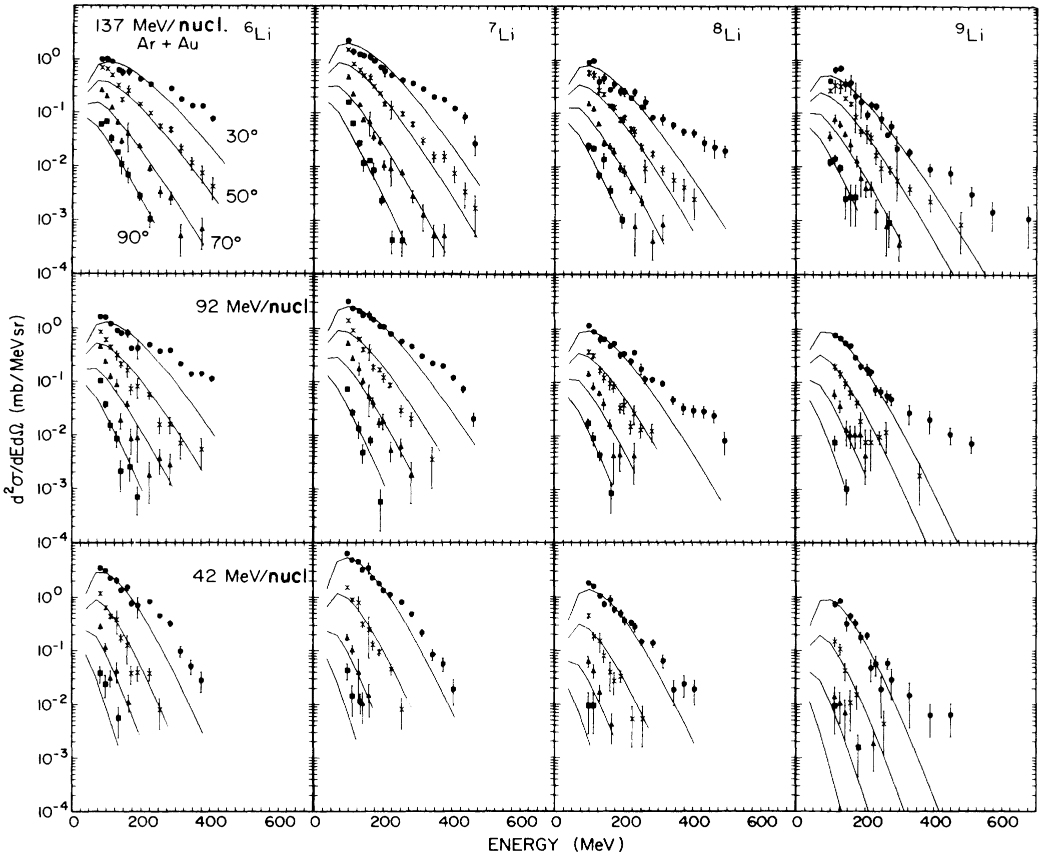

FIG. 8. Double differential cross sections for lithium isotopes produced in Ar + Au reactions at 137, 92, and 42 MeV/nucleon. Data at 30°, 50°, 70°, and 90° are shown for each particle. The solid lines are fits with a single moving source parametrization.

sources to become close together and difficult to separate.

For the Ar + Ca system, the projectile and target are indistinguishable in the center of mass reference frame and the contours may be reflected about the rapidity of the center of mass. Figure 18 shows a Lorentz-transformed plot in which $y = 0$ corresponds to the center of mass rapidity, and the information given by the data points in the lower left section of Fig. 18 has been reflected through the center of mass rapidity. The contours have been drawn smoothly through the measured and reflected data points and show the contributions from various sources of particles. Protons associated with the projectile and target are visible in the contours as bumps centered about the corresponding rapidities y and y_t. The remaining contours indicate proton emission from a source moving with approximately the center of mass rapidity.

The rapidity plots for ^{7}Be produced in the Ar + Au and Ar + Ca reactions are presented in Fig. 19 for comparison with the light fragment results. Comparison of the observed contours with the dashed circles for target emission and the dot-dashed circles for the intermediate rapidity source show that beryllium fragments arise from an intermediate rapidity as well as target source as was the case for light particles.

IV. SINGLE MOVING SOURCE PARAMETRIZATION

A. Rationale

The high energy tails ($E > 40$ MeV/nucleon) of the spectra shown in Figs. 4—16 can be rather well described in terms of a Maxwellian distribution observed in a moving frame. Such a distribution would result if the particles were emitted from a thermalized gas of nucleons. The solid lines in these figures show a parametrization of the high energy, exponential region of the spectra in terms of emission from a single, thermalized source. The slopes of the spectra indicate a large excitation energy, and the angular distributions suggest that the source moves in the laboratory frame. In contrast, the low energy portions of the spectra suggest emission from a cooler region almost stationary in the laboratory frame. Similar spectral shapes and angular distributions in relativistic heavy ion

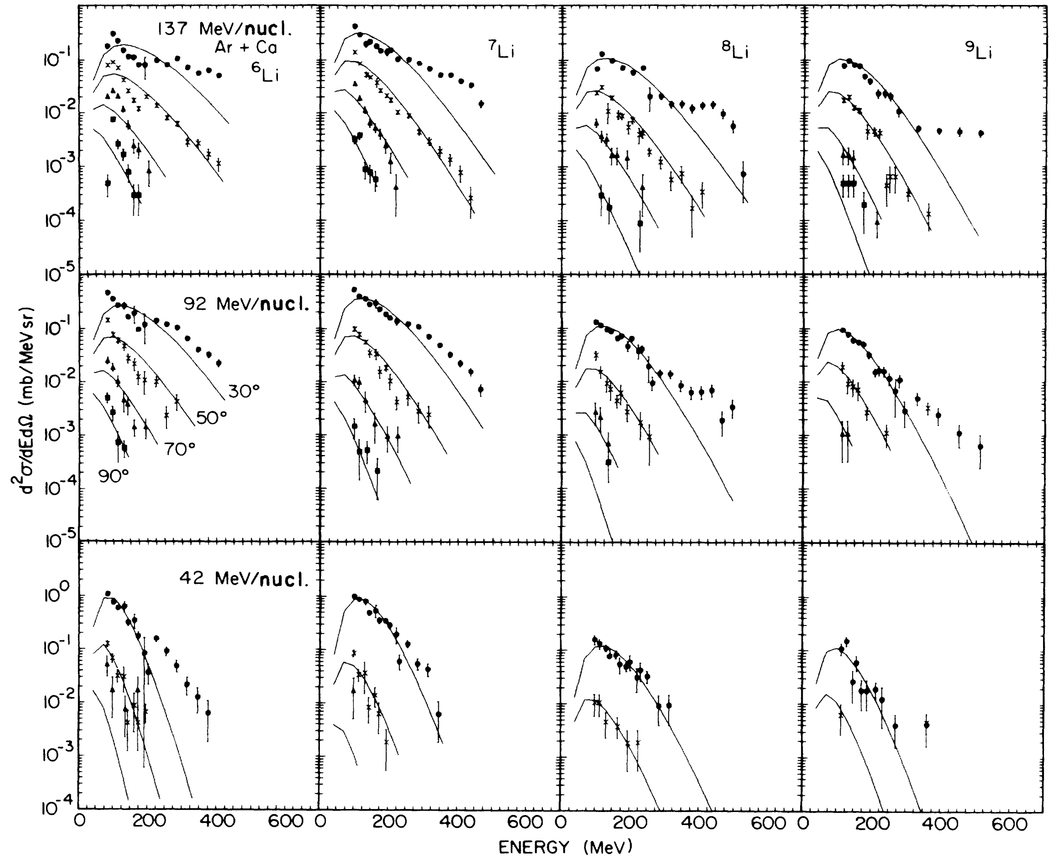

FIG. 9. Double differential cross sections for lithium isotopes produced in Ar + Ca reactions.

collisions have led to the participant-spectator or fireball picture of nuclear collisions.[24] In this model, the reaction is described in terms of a highly excited participant region, or fireball, consisting of nucleons present in the overlap of the projectile and target, and the cold spectator remnants of the target and projectile.

A single source parametrization has been used to characterize emission of nucleons and composite fragments from the participant region.[5] The concept of dividing the reaction (and the resulting energy spectra) into major regions has been applied for bombarding energies as low as 10 MeV/nucleon.[10] The moving source parametrization is clearly an oversimplification of the reaction mechanism. There are certainly a continuum of sources for intermediate rapidity fragments, but we use this parametrization based on formation of such a region in order to compare various sets of data and explore the evidence for thermalization. The high energy tails of the spectra have been successfully described by emission from a single moving source, and the extracted parameters vary smoothly from 10 to 2000 MeV/nucleon.[14,33]

B. Fitting procedure

In order to isolate the component of the inclusive spectra originating from an intermediate velocity source, a selection criterion in the spectra was established. Projectile fragments populate forward angles near the projectile velocity. We therefore associate light particles (p, d, t, ^{3}He, ^{4}He, and ^{6}He) emitted at angles $\geq 50°$ with an intermediate source. Heavier fragments at angles $\geq 30°$ are included in the fits. Target fragmentation leads to low energy particles distributed almost isotropically in the laboratory frame.

Figure 20 illustrates the relative contributions of particles from different sources to the inclusive energy spectra. The sizes of the projectile, target, and intermediate sources of protons from 137 MeV/nucleon Ar + Au were estimated using the cleancut geometry of the fireball model at the most probable impact parameter.[5,32] The dashed lines show the energy spectra of protons emitted by a source with 30 MeV temperature moving at a velocity 0.45 times the beam velocity. The solid lines show the energy spectra obtained by summing the spectra from the intermediate source with the spectra expected for protons emitted from the projectile and target remnants with temperatures of 8 MeV. It is evident that the inclusive spectra at angles $>40°$ and $E > 50$ MeV consist primarily of particles emitted from the intermediate source.

We have determined the intermediate source parameters from the observed spectra by describing the energy distribution in the source with a relativistic Boltzmann distri-

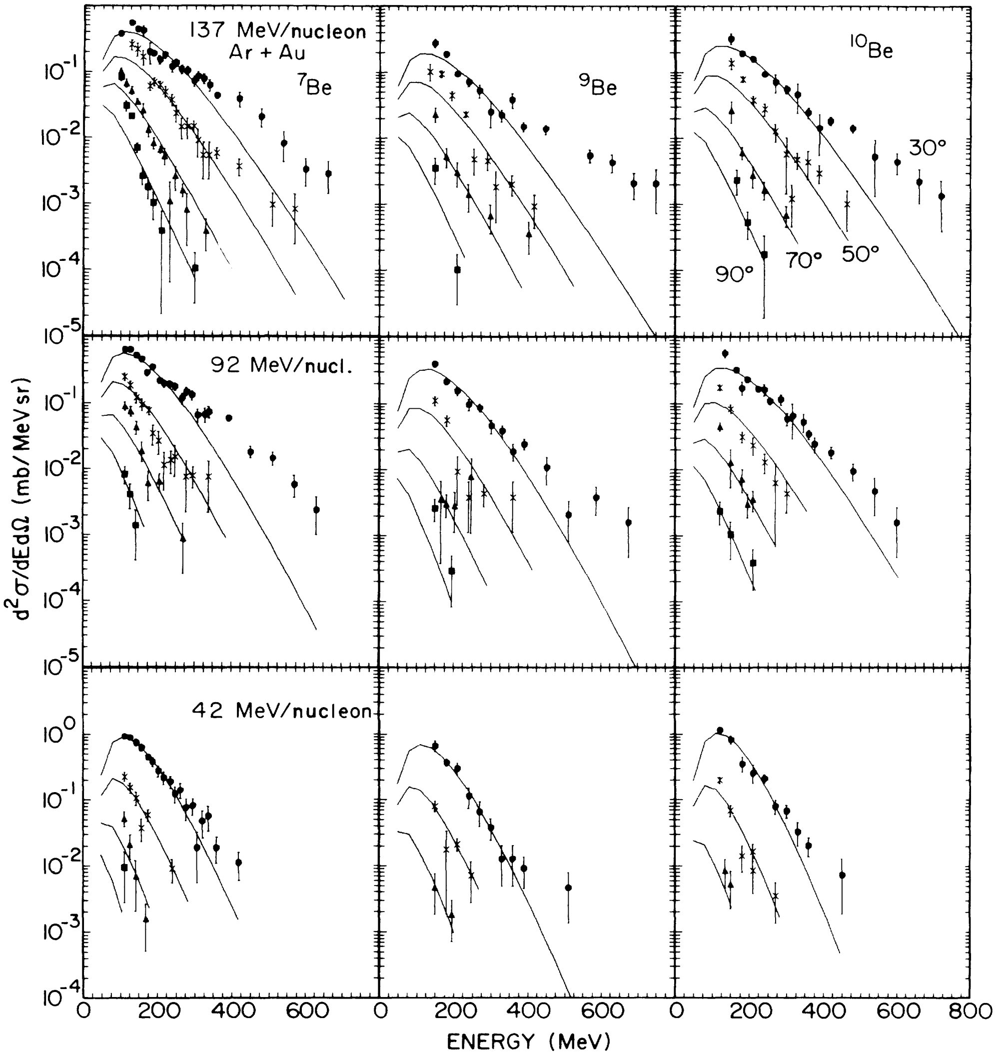

FIG. 10. Double differential cross sections for beryllium isotopes produced in Ar + Au reactions.

bution of the form[52]

$$\frac{d^2}{p^2dp\,d\Omega}=\frac{\sigma_0}{(4\pi)^3}\frac{e^{-E/\tau}}{2(\tau/m)^2K_1(m/\tau)+(\tau/m)K_0(m/\tau)}\ , \tag{5}$$

where p and E are the momentum and total energy of a particle in the source rest frame. The particle mass is given by m, σ_0 is the production cross section, and τ is the source temperature. K_0 and K_1 are MacDonald functions.[53]

The distribution is assumed to be isotropic in a frame moving with the velocity β in the laboratory frame. The laboratory spectra of particles emitted from the source are obtained by transforming relativistically from the source rest frame to the laboratory using

$$\frac{d^2\sigma}{dE\,d\Omega}=pE'\frac{d^2\sigma}{p'^2dp'\,d\Omega'}\ , \tag{6}$$

where $E'=\gamma(E-\beta p\cos\theta)$ and $\gamma=1/(1-\beta^2)^{1/2}$. The primed quantities refer to the source frame and the unprimed quantities refer to the laboratory frame. The parameters σ_0, τ, and β are determined by using a least squares method to fit that part of the measured spectra identified with the intermediate source.

The value of the low energy cut to exclude particles arising from the target was determined by iteratively fitting the data, raising the energy cut until the fit parameters no longer changed. The low energy cutoffs for light particles in experiments reported in this paper are given in Table III. All measured heavy fragments were used for the moving source fits.

A correction for the Coulomb interaction between the observed fragment and the charged emitting region was used in the fitting procedure. We assumed that particles are emitted from a subsystem containing the nucleons present in the projectile-target overlap region in a collision at the most probable impact parameter, and that the particles come out late enough in the collision that the system

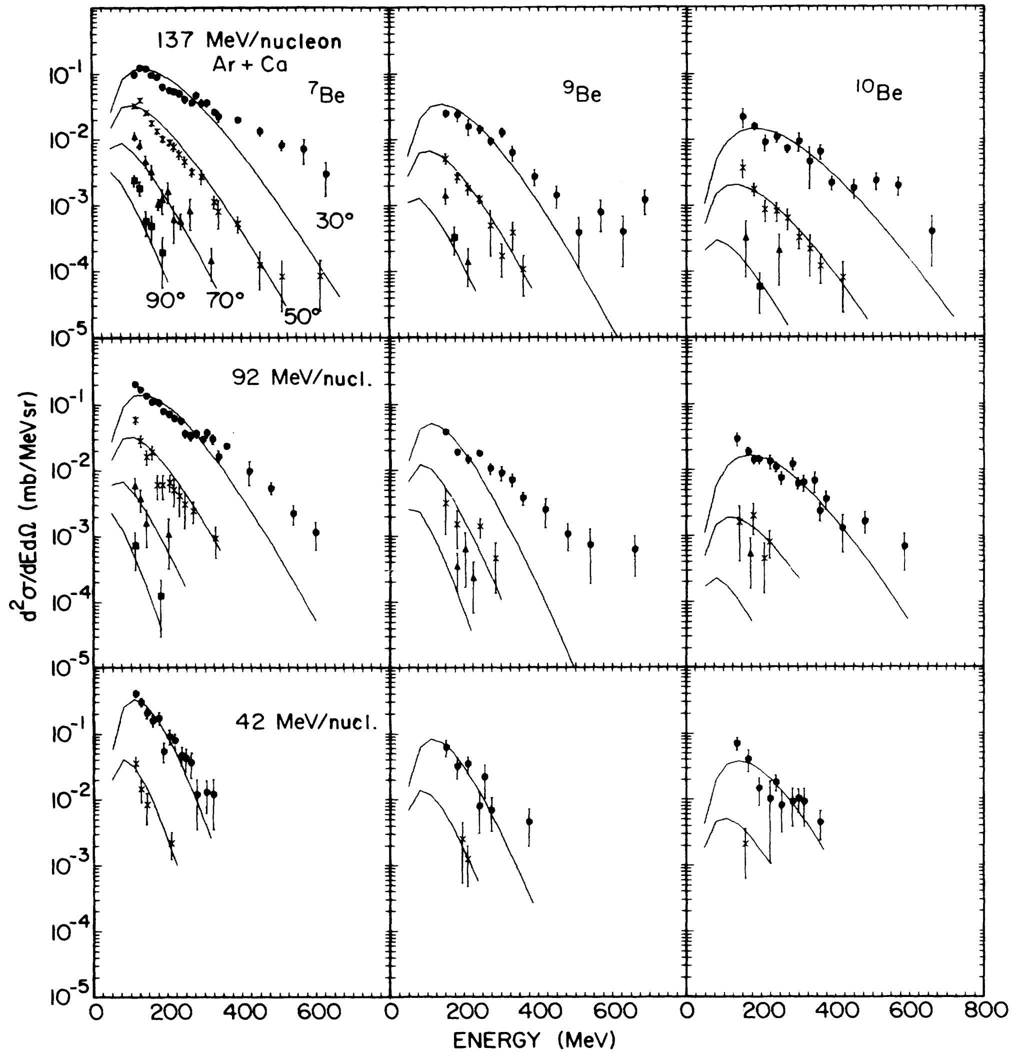

FIG. 11. Double differential cross sections for beryllium isotopes produced in Ar + Ca reactions.

is separated in space from the target remnant. We have further simplified the Coulomb correction by performing it in the laboratory rather than in the rest frame of the intermediate source. The correction was applied by shifting the calculated spectrum back by the amounts shown in Tables IV and V. The fits are rather insensitive to small changes in the Coulomb shift applied. We have compared the parameters obtained using our fitting procedure[14] with the non-relativistic procedure used by other authors.[10,26] The parameters agree within error bars in those cases where both fitting prescriptions have been done on the same data set.

C. Limitations

The best fits with the moving source prescription are shown as the solid lines in Figs. 4—16. For light particles ($1 \leq A \leq 4$) the 30° spectra are consistently underpredicted which results from the fact that these spectra include substantial contributions from decay of projectile fragments. When the spectra of light particles emitted from the projectile fragments are transformed to the laboratory frame, some are observed at 30°, as schematically illustrated in Fig. 20. Because of this projectile contribution we do not expect single source emission to reproduce the 30° spectra, and do not include these data when determining the parameters. The contribution from low energy fragments associated with decay of an excited residual target nucleus was minimized by the choice of the thickness of the front element of the Si detector telescopes.

The 30° spectra for fragments with $E > 43$ MeV/nucleon are quite flat and cannot be described by emission from a single source. This effect is observed at all three bombarding energies and for both targets. In the fits for lithium and heavier fragments, it is difficult to reproduce the energy spectra below 150 MeV. The heavier fragment spectra do not show an obvious break in slope, but the ability to reproduce the high energy tails

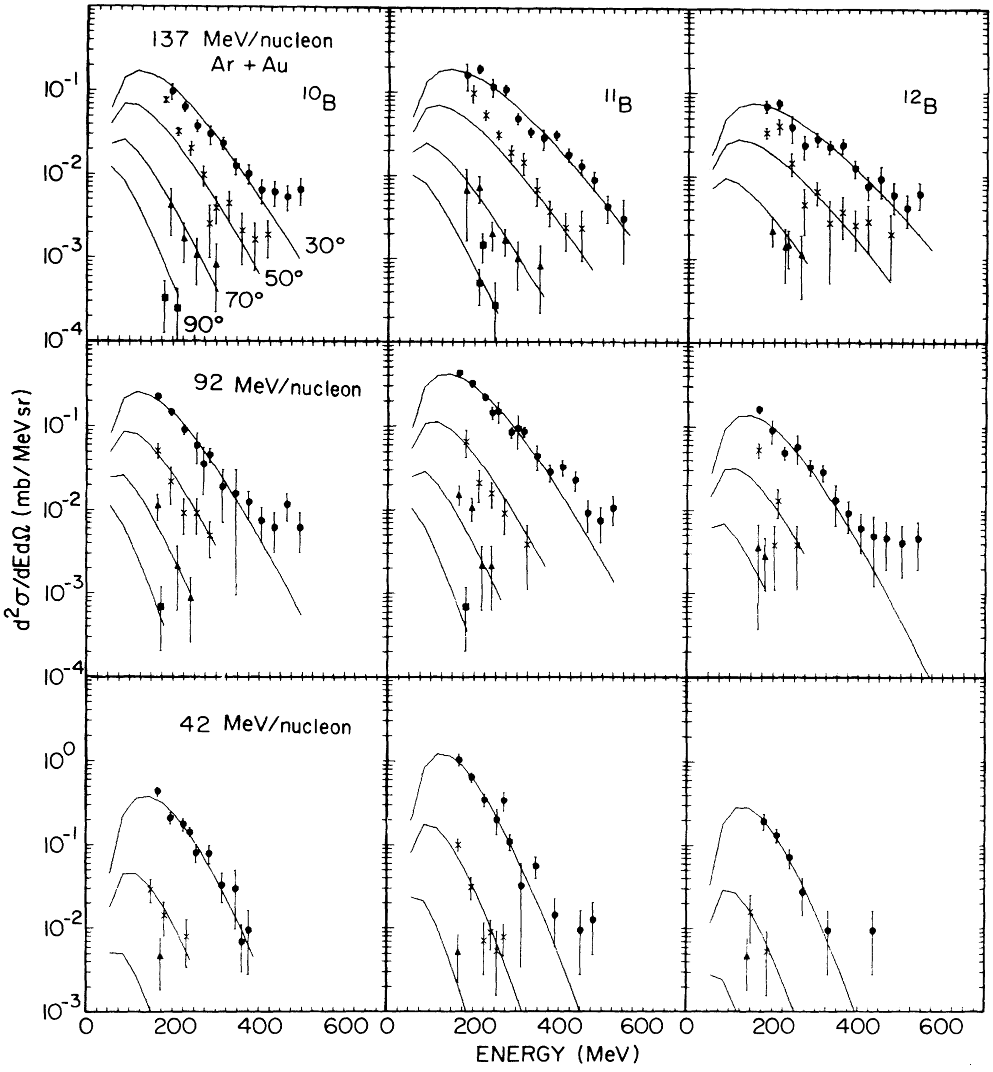

FIG. 12. Double differential cross sections for boron isotopes produced in Ar + Au reactions.

with a single source and the difficulty with the low energy fragments suggests that fragment emission may also be a superposition of target and participant sources. Full characterization of the participant source is difficult due to the low cross sections at back angles. At 42 MeV/nucleon, the measured spectra at angles larger than 30° extend less than 200 MeV past the target evaporation region, which emphasizes the difficulty in separating the fragment sources at low bombarding energies and the necessity of measuring the particles in the high energy tails of the spectra to identify fragments arising from the participant zone.

D. Discussion of parameters

The values of the three moving source parameters, the temperature τ, the source velocity β, and the production cross sections σ_0, are given in Tables VI—VIII. Results for Ar + Au reactions are in Table VI, for Ar + Ca in Table VII and for the Ne-induced reactions in Table VIII. Figure 21 shows the temperatures extracted from the spectra for each particle observed in the Ar-induced reactions.[22] These temperatures are considerably higher than those expected for a compound nucleus, and increase with bombarding energy. The temperatures for light particles from Ar + Ca are comparable to those from Ar + Au, and the heavier fragment temperatures for Ar + Ca are systematically lower by a few MeV.

The most apparent feature of the figure is the lack of variation of the temperature with fragment mass. The fluctuations in the temperatures from 137 MeV/nucleon reactions may be due to the fact that the heavy fragment telescopes only measured particles up to 80 MeV/nucleon, thus sampling only a portion of the intermediate rapidity data. The similarity of the temperature over the measured range of fragment masses suggests that the fragments originate from a thermal source, and that the same type of

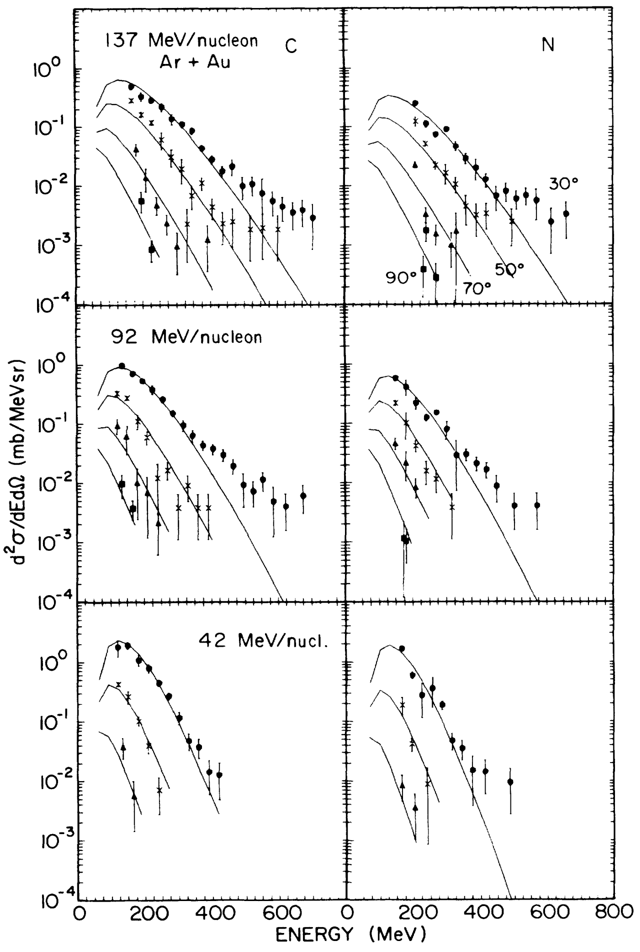

FIG. 13. Double differential cross sections for carbon and nitrogen fragments produced in Ar + Au reactions.

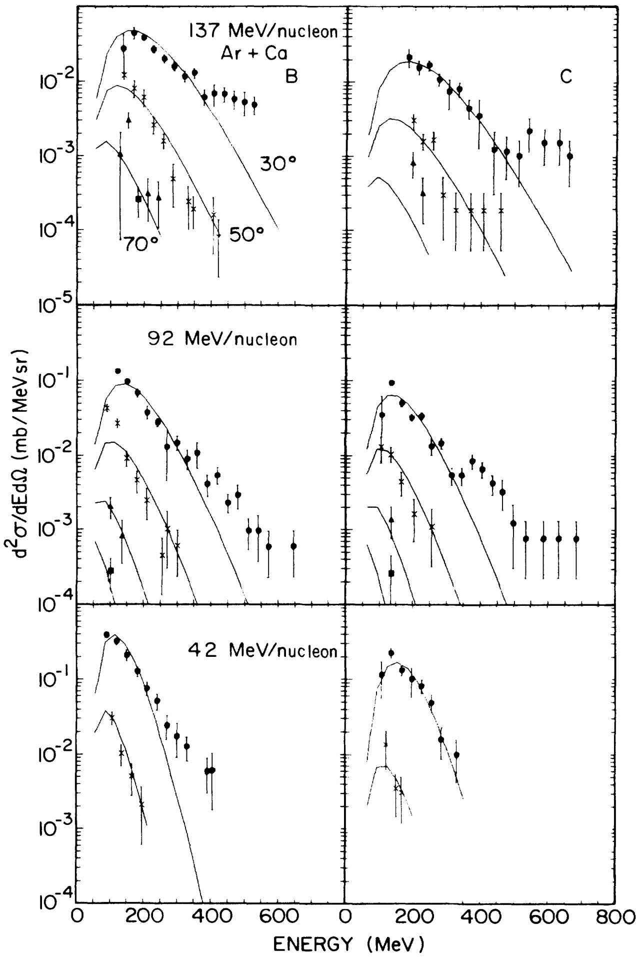

FIG. 14. Double differential cross sections for boron and carbon fragments produced in Ar + Ca reactions.

source gives rise to the heavy and the light fragments. It would be difficult to account for the production of $A=14$ fragments at intermediate rapidity by only a few nucleon-nucleon scatterings. Therefore the trends of the temperatures support the idea of thermalization of the emitting system.

Figure 22 shows the velocity parameter of the emitting source (expressed as a fraction of the projectile velocity), again plotted as a function of the fragment mass. This parameter depends strongly on the angular distribution of the observed particles, and is the least well determined of the three parameters. This dependence is particularly strong for the heavy fragments, where spectra at only four angles were measured.

The velocities extracted from the light particle spectra are approximately half the projectile velocity for Ar + Ca, and somewhat lower for Ar + Au. These values correspond to equal numbers of projectile and target nucleons expected in the overlap region for Ar + Ca collisions, and to the excess of target nucleons in Ar + Au. As the fragment mass increases, the velocity decreases, possibly due to limitations in the measured angular distribution. It is, however, likely that the lower velocity reflects a more central collision. In such a collision, a larger thermal system would be created, with enough nucleons to emit a heavy fragment, and with a lower velocity in the laboratory due to a higher fraction of target nucleons. Another possibility is that the heavy fragments are emitted from a later stage in the reaction than the light particles, after a fraction of the energy from the participant region has been absorbed by the spectator region.

The third parameter, σ_0, is the production cross section for each type of particle. This cross section corresponds to emission from the intermediate rapidity source, excluding particles originating from the projectile and target. Figures 23 and 24 show the values of this parameter as a function of the fragment mass for Ar + Au and Ar + Ca reactions, respectively. The cross sections fall approximately exponentially with fragment mass and the distribution becomes slightly steeper as the bombarding energy is increased.

The fragment distributions resulting from integration of the measured spectra (extrapolated to all energies and angles) look approximately the same as shown in Figs. 23

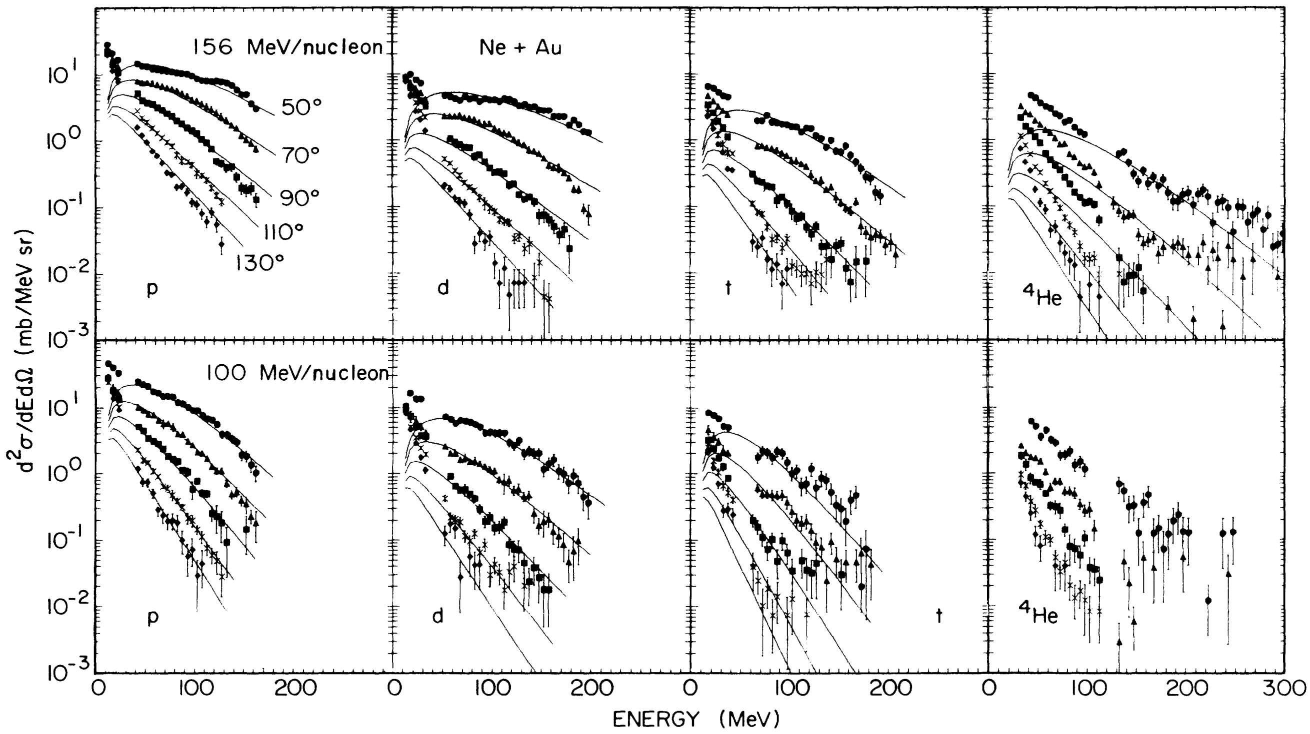

FIG. 15. Double differential cross sections for p, d, t, and ^{4}He from Ne + Au reactions at 156 and 100 MeV/nucleon. Data at 50°, 70°, 90°, 110°, and 130° are shown. The solid lines are fits with a single moving source parametrization.

and 24. The error bars in the figures reflect the differences between the integrated single source cross section and the extrapolation of the measured spectra.

Figure 25 provides a comparison of fragment production for the different targets and bombarding energies. The cross section ratios of composite fragments and protons are plotted up to ^{9}Li. These ratios fall with increasing fragment mass, but exhibit an enhancement at ^{4}He due to its large binding energy. This enhancement is prominent at 42 MeV/nucleon, where the excitation energy of the system is relatively low. The shapes of the distributions are very similar for both the Au and Ca targets, with the formation of composites slightly less probable in Ar + Ca reactions.

In Fig. 26 the projectile dependence of the extracted source parameters is presented. Reactions of Ne and Ar projectiles with Au targets at approximately the same bombarding energies are compared. The temperatures

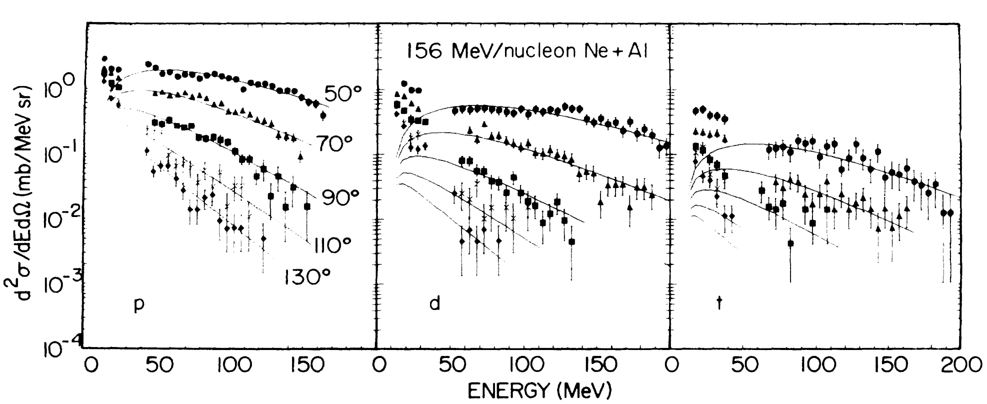

FIG. 16. Double differential cross sections for p, d, and t from 156 MeV/nucleon Ne + Al. Data at 50°, 70°, 90°, 110°, and 130° are shown for each particle. The solid lines are fits with a single moving source parametrization.

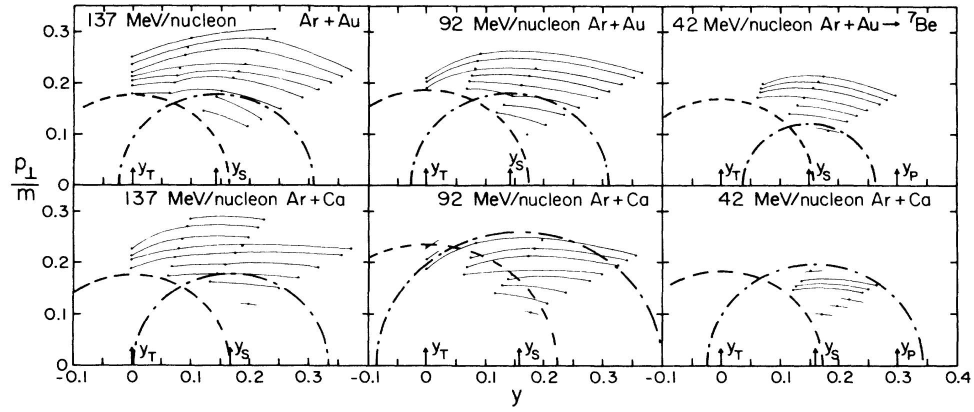

FIG. 17. Contours of constant cross section in the rapidity versus perpendicular momentum plane for protons produced in Ar + Au and Ar + Ca reactions. Dashed semicircles indicate contours expected for emission from a target-like source and dot-dashed semicircles indicate contours from a midrapidity source.

and velocities describing the triton and ^{4}He spectra are roughly comparable to the proton and deuteron parameters in the case of Ar-induced reactions, but fall with increasing fragment mass in Ne-induced reactions. This decrease may reflect a smaller interaction region in Ne-induced reactions, leading to a larger target-like source contribution to the triton and ^{4}He spectra. The particles emitted from the target would cause the extracted temperatures and velocities to look lower than if the fitted spectra consisted purely of particles from the intermediate rapidity source.

E. Systematics of the temperature

The excitation energy of the source, given by the temperature parameter and the relative numbers of nucleons and complex nuclei, should vary smoothly with incident energy if a local, thermalized zone is formed. In fact, the parameters in the simple one-source description do vary smoothly with bombarding energy.[14] Source temperatures extracted using proton spectra from reactions at 10—2100 MeV/nucleon (Refs. 6, 7, 10, 12, and 14) are shown in Fig. 27.

The circles represent temperatures extracted from proton spectra from O- and Ne-induced reactions on heavy targets. Temperatures resulting from the present data for Ar + Au and Ne + Au data are shown as squares and triangles, respectively. The solid line shows the temperature expected for the participants if the projectile and target cut cleanly and the nucleons in the overlapping region come to thermal equilibrium. This temperature is calculated via the fireball model described in the next section and includes pion production which causes the flattening of the line above 400 MeV/nucleon.[54] The dashed line shows the temperature expected for an ideal Fermi gas of nucleons.

The regularity of the temperature parameter as a function of bombarding energy observed over this range of incident energies supports the idea that a subset of the nucleons in the projectile and target are involved in a

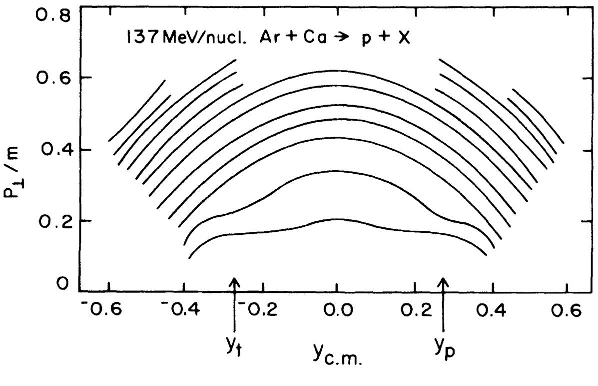

FIG. 18. Rapidity plot for protons from Ar + Au at 137 MeV/nucleon presented in the center of mass frame. The contours at high rapidity were obtained by assuming forward-backward symmetry.

TABLE III. Low energy cutoffs for moving source fits to spectra.

Particle	Ar + Au (MeV)	Ar + Ca (MeV)	Ne + Au (MeV)	Ne + Al (MeV)
p	52.5	52.5	37.5	37.5
	52.5	42.5[a]		
d	85	85	42.5	42.5
	85	65[a]		
t	67.5	67.5	42.5	42.5
	67.5	52.5[a]		
^{3}He	112.5	112.5	57.5	57.5
	52.5	52.5[a]		
^{4}He	150	150	101.5	101.5
	70	70[a]		
^{6}He	135	135		
	135	75[a]		

[a] For 42 MeV/nucleon.

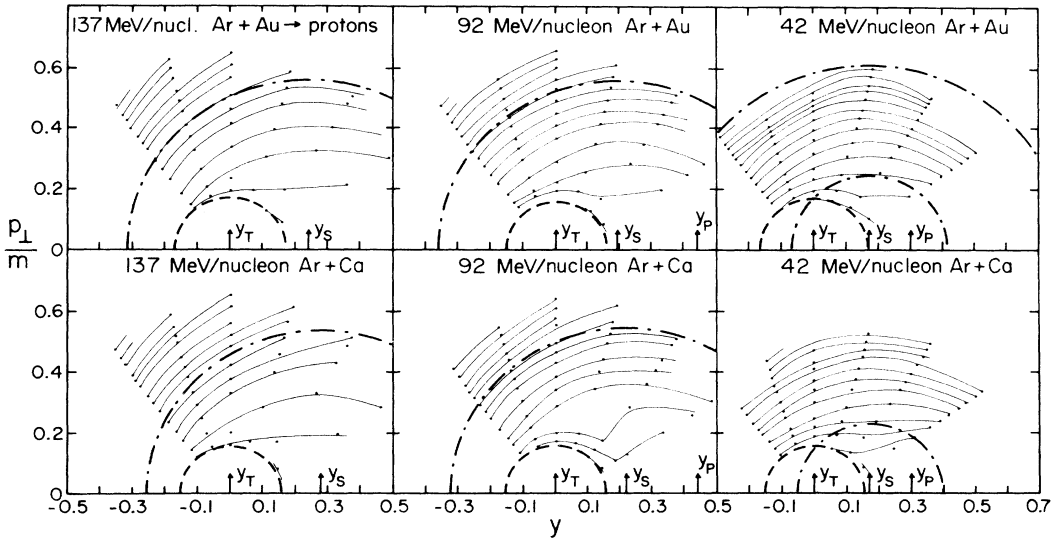

FIG. 19. Same as Fig. 17 for ^{7}Be.

thermalized region during the reaction. The temperatures deduced from the spectra are similar to those expected for such a thermalized system, resembling a Fermi gas at low energies, and including pion production at higher energies. Several models of the reaction mechanism incorporating a thermalization step are discussed in the next section.

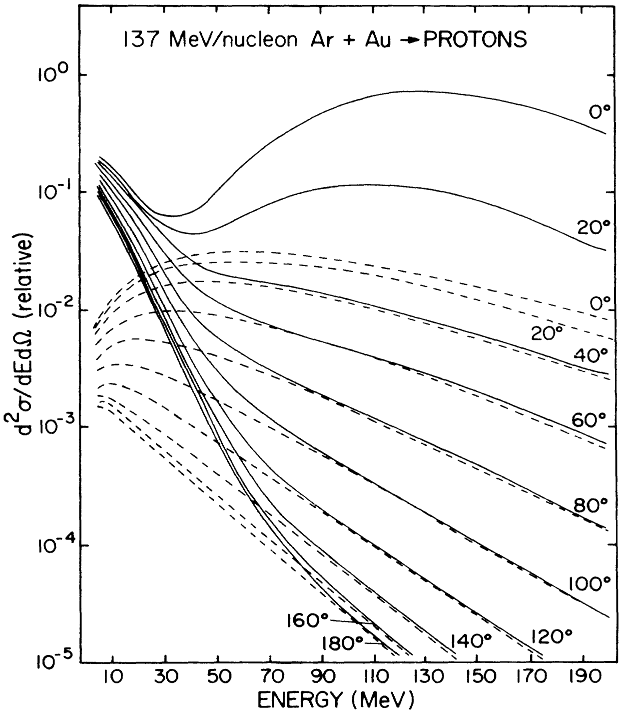

FIG. 20. Schematic proton spectrum for 137 MeV/nucleon Ar + Au, calculated from complete disassembly of the fireball at the most probable impact parameter (dashed lines) and disassembly of the fireball plus spectator fragments (solid lines).

F. Three moving sources

In order to further investigate the applicability of the participant-spectator picture of reactions at these bombarding energies, we have fitted the light particle data from 137 MeV/nucleon Ar + Au assuming emission from three sources. One source is the intermediate source, analogous to the single moving source described above. The other two sources treat emission of light particles from the relatively cool spectator fragments. We include a projectile-like source, moving with the original projectile velocity and with a temperature of 8 MeV. The target evaporation spectrum is accounted for with a slow source, moving with approximately the compound nuclear velocity.

When fitting the data, it was necessary to hold some of the parameters fixed. The projectile source, for example, was not sufficiently defined by the measured data as we have no information forward of 30°. We therefore held the velocity of this source fixed at the projectile velocity, and the temperature fixed at 8.0 MeV. For the protons, the cross section for the projectile-like source was a fitted parameter, but for the other particles we were obliged to hold this parameter fixed as well. For these cases the fit-

TABLE IV. Coulomb shifts used in moving source fits to spectra of particles from Ar-induced reactions.

Particle	Ar + Au (MeV)	Ar + Ca (MeV)
H	10.0	4.5
He	18.0	8.0
Li	25.0	11.2
Be	34.0	14.7
B	40.0	18.0
C	48.0	21.0
N	55.0	24.0

TABLE V. Coulomb shifts used in moving source fits to spectra of particles from Ne-induced reactions.

Particle	Ne + Au (MeV)	Ne + Al (MeV)
p	10	10
d	10	10
t	10	10
^{4}He	18	18

ting was done by iteratively changing the cross section, and subsequently choosing the fit with the best χ^2 value. The fits were not, however, very sensitive to the cross section of the projectile-like source.

We also fixed the velocity of the target-like source. The upper limit of the recoil of the target-like source was estimated to be the velocity expected for the compound nucleus. The target-like source temperature and cross section were fitted parameters, and the temperatures were found to be somewhat lower than 8 MeV.

Within these limitations, we were able to obtain fits for protons through ^{3}He. We were not able to fit the ^{4}He spectra, even when holding the spectator source parameters fixed. It is possible that the lack of forward angle and very low energy data reduced our knowledge of the alpha emission from the spectator sources so that the three source fit was not significantly better than the single source fit.

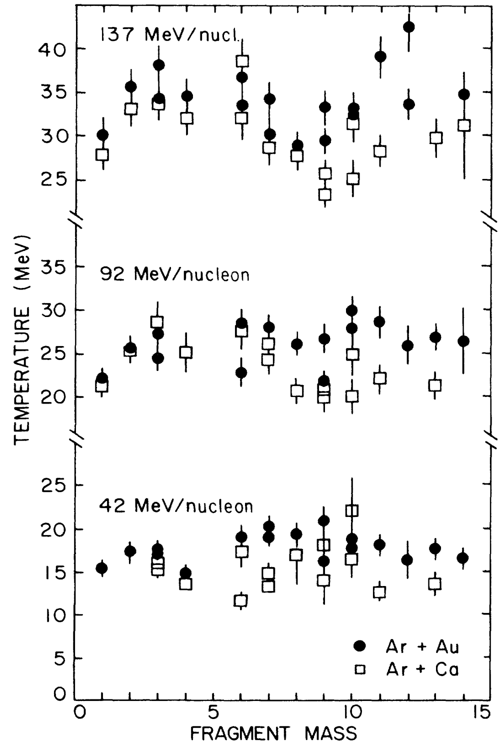

FIG. 21. Temperatures extracted from the spectra of fragments emitted from Ar-induced reactions, as a function of the fragment mass.

Figure 28 shows the three source fits for protons, deuterons, and ^{3}He from 137 MeV/nucleon Ar + Au. It is clear that the fits are much closer to the data at forward angles and low energies than the single moving source fit because particle emission from the spectators is taken into account. The extracted source parameters are given in Table IX. The parameters of the intermediate source in the three source fit are very similar to the parameters extracted for the intermediate rapidity source in the single moving source fit. This result supports the usefulness of the single source parametrization of the intermediate rapidity data and gives us confidence in the selection criteria applied when making those fits.

V. THERMAL MODELS

A. The fireball model

As data from relativistic heavy ion collisions became available, a variety of models to explain the reactions were formulated. Intranuclear cascade models treat the reaction as a superposition of nucleon-nucleon collisions. In hydrodynamical models the nucleons are assumed to have a very short mean free path and nuclear matter is treated as a compressible fluid. These models will be discussed in more detail in Sec. VI. Thermal models assume that an equilibrated system is formed during the reaction and ascribe a density and hadronic temperature to the matter during the collision . The fireball model[5,23,54] predicts such quantities by using an idealized geometry for the re-

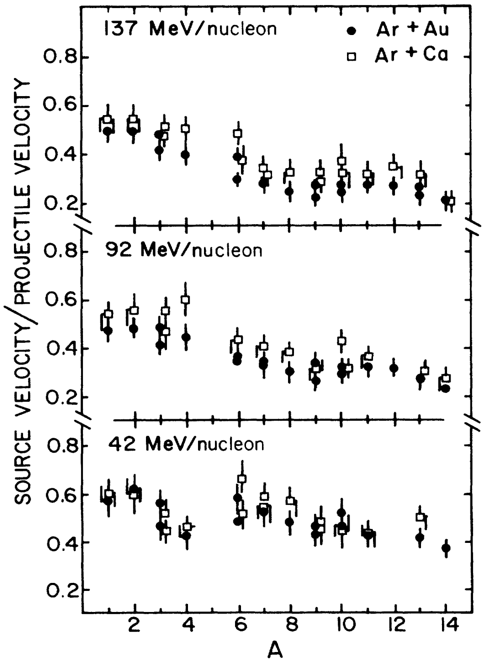

FIG. 22. The ratio of the source velocity extracted from fragment spectra to the projectile velocity for Ar-induced reactions as a function of the fragment mass.

TABLE VI. Moving source parameters extracted for Ar + Au reactions.

	137 MeV/nucleon			92 MeV/nucleon			42 MeV/nucleon		
Particle	τ (MeV)	σ_0 (mb)	β	τ (MeV)	σ_0 (mb)	β	τ (MeV)	σ_0 (mb)	β
p	30.2	40 400	0.24	22.1	26 100	0.19	15.5	36 800	0.17
d	35.6	19 500	0.24	25.7	13 800	0.20	17.5	22 000	0.18
t	34.2	10 100	0.20	24.5	6810	0.17	17.7	12 300	0.16
^{3}He	38.2	3140	0.23	27.3	2100	0.20	17.3	3740	0.13
^{4}He	34.5	4120	0.19	25.1	3050	0.18	15.0	22 900	0.12
^{6}He	36.8	820	0.19	22.8	910	0.15	19.1	1540	0.17
^{6}Li	33.5	410	0.14	28.6	500	0.14	19.1	820	0.14
^{7}Li	30.2	810	0.13	28.2	970	0.14	19.1	1640	0.15
^{8}Li	29.0	300	0.12	26.2	330	0.12	19.4	420	0.14
^{9}Li	29.5	200	0.10	21.9	270	0.11	16.3	246	0.12
^{7}Be	34.3	180	0.14	28.0	215	0.14	20.3	280	0.15
^{9}Be	33.3	86	0.13	26.8	130	0.14	21.0	225	0.13
^{10}Be	33.2	110	0.13	30.0	150	0.14	17.8	335	0.13
^{10}B	32.7	75	0.12	28.0	97	0.12	18.8	150	0.15
^{11}B	39.1	100	0.13	28.7	180	0.14	18.1	420	0.13
^{12}B	42.5	36	0.13	26.0	56	0.13	16.4	110	0.13
C	33.6	240	0.11	27.0	340	0.11	17.7	710	0.12
N	34.8	125	0.10	26.4	220	0.09	16.6	550	0.12

TABLE VII. Moving source parameters extracted for Ar + Ca reactions.

	137 MeV/nucleon			92 MeV/nucleon			42 MeV/nucleon		
Particle	τ (MeV)	σ_0 (mb)	β	τ (MeV)	σ_0 (mb)	β	τ (MeV)	σ_0 (mb)	β
p	27.8	23 400	0.27	21.4	14 400	0.22	15.5	16 100	0.17
d	33.1	9750	0.27	25.2	5840	0.23	16.9	6600	0.17
t	34.1	3260	0.23	24.2	1850	0.19	16.2	2490	0.15
^{3}He	33.6	2010	0.25	28.8	820	0.23	15.5	2090	0.13
^{4}He	32.0	1870	0.25	25.1	1490	0.25	13.8	6220	0.13
^{6}He	38.7	305	0.24	23.0	280	0.18	17.4	415	0.19
^{6}Li	32.0	77	0.18	27.7	100	0.18	11.8	245	0.15
^{7}Li	28.6	110	0.15	24.4	135	0.17	13.4	320	0.17
^{8}Li	27.9	39	0.16	20.8	38	0.16	17.0	43	0.17
^{9}Li	23.3	32	0.14	20.0	28	0.13	14.1	29	0.13
^{7}Be	30.8	46	0.17	26.1	55	0.16	14.7	91	0.16
^{9}Be	25.6	12	0.16	20.8	15	0.13	18.2	24	0.14
^{10}Be	31.4	8	0.18	26.4	9	0.18	22.0	15	0.16
B	28.3	19	0.15	22.1	33	0.14	12.7	105	0.12
C	29.7	9	0.15	21.4	22	0.12	13.6	77	0.15

TABLE VIII. Moving source parameters extracted for Ne-induced reactions.

	156 MeV/nucleon Ne + Au			100 MeV/nucleon Ne + Au			156 MeV/nucleon Ne + Al		
Particle	τ (MeV)	σ_0 (mb)	β	τ (MeV)	σ_0 (mb)	β	τ (MeV)	σ_0 (mb)	β
p	32.1	10 500	0.24	22.5	11 400	0.21	31.5	1650	0.29
d	34.9	4860	0.23	25.6	4780	0.20	34.2	643	0.27
t	26.7	1940	0.16	17.8	1930	0.13	29.9	127	0.19
^{4}He	25.6	995	0.15	14.2	3690	0.16			

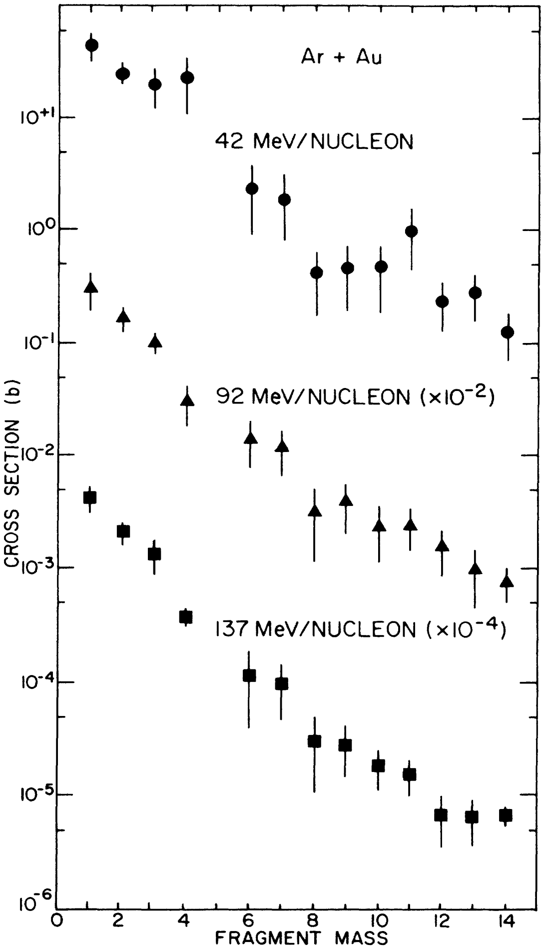

FIG. 23. The integrated fragment production cross sections for Ar + Au as a function of the fragment mass.

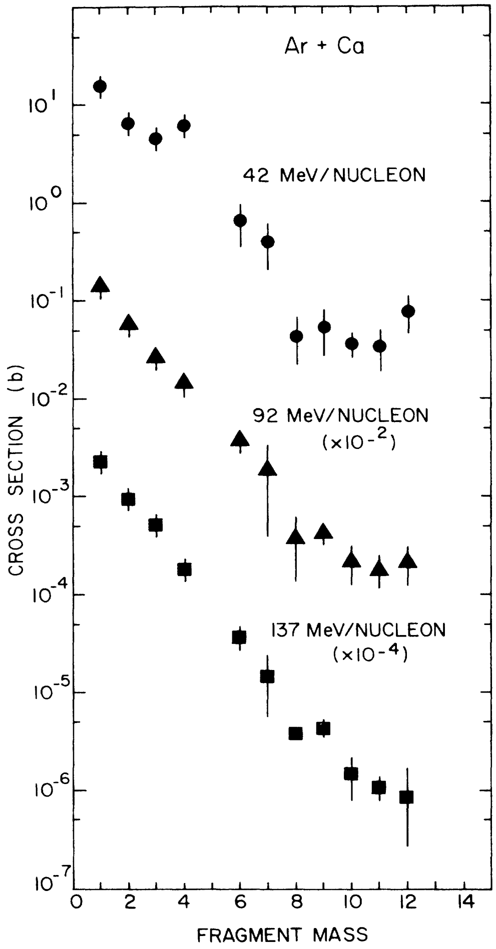

FIG. 24. The integrated fragment production cross sections for Ar + Ca as a function of the fragment mass.

action and statistical formulations of the state of the system.

In the fireball model there is a fast primary reaction stage where the interaction is localized to the overlapping volume of target and projectile nuclei. Later, the excitation energies of the remnants of the two spectator nuclei are dissipated by the emission of particles and gamma rays. The excitation energy of the remnants is relatively low, so the particles from the remnants have lower energies than those from the participants. The nuclear fireball consists of the nucleons contained in the region formed via cylindrical cuts swept out of the target by the projectile and the projectile by the target in the primary part of the reaction. The projectile nucleons transfer all of their momentum into excitation energy of the fireball which moves forward in the lab at a velocity intermediate between those of the projectile and target. The fireball is treated as an equilibrated nonrotating ideal gas and the excitation energy and velocity are calculated from the number of nucleons contributed by the projectile and target to the participant region.

The lab inclusive spectra are calculated by summing over impact parameters and letting the fireball with temperature τ and velocity β emit particles with energies given by a relativistic Boltzmann distribution in the fireball rest frame. It is assumed that chemical as well as thermal equilibrium is achieved in the fireball and composite fragments as well as that protons are emitted. The calculated spectra are the sum of bound nuclei and decay products from particle unstable nuclear and baryonic resonances. The relative cross sections for protons and composites are determined by the temperature and the numbers of neutrons and protons in the system, the binding energies of the composites, and the density at which the fragments no longer interact. The density used in the present calculation is $\rho = 0.8\rho_0$, but the results are relatively insensitive to ρ for $0.5\rho_0 < \rho < 1.5\rho_0$.

Figure 29 shows the results of a fireball calculation for proton, deuteron, and ^{3}He spectra observed in the 137 MeV/nucleon Ar + Au reaction. The nuclei in the chemical equilibrium are truncated at $A = 5$, resulting in unreliable predictions for ^{4}He production. The solid lines show the results of the calculation at 30°, 50°, 70°, 90°, 110°, and 130° in the laboratory. The agreement between

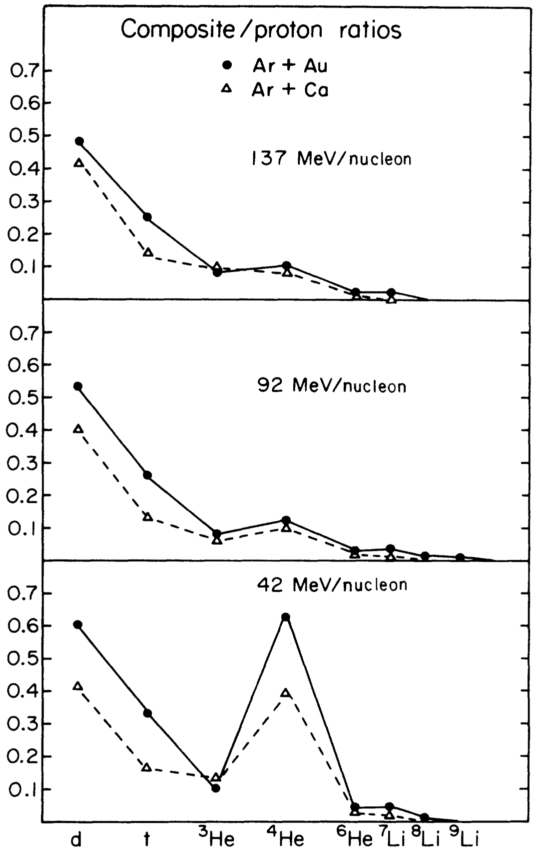

FIG. 25. The ratio of composite fragment cross sections to the proton cross sections for Ar-induced reactions on Au and Ca targets.

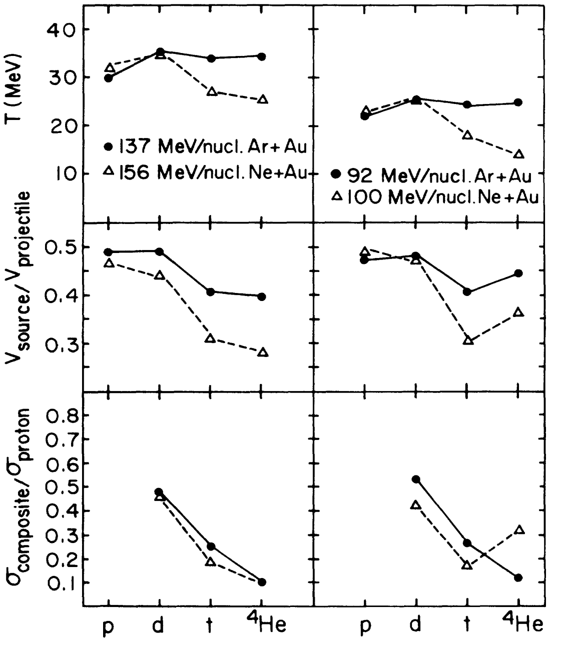

FIG. 26. Projectile dependence of the moving source parameters describing light particle spectra, for Ar and Ne beams on Au targets.

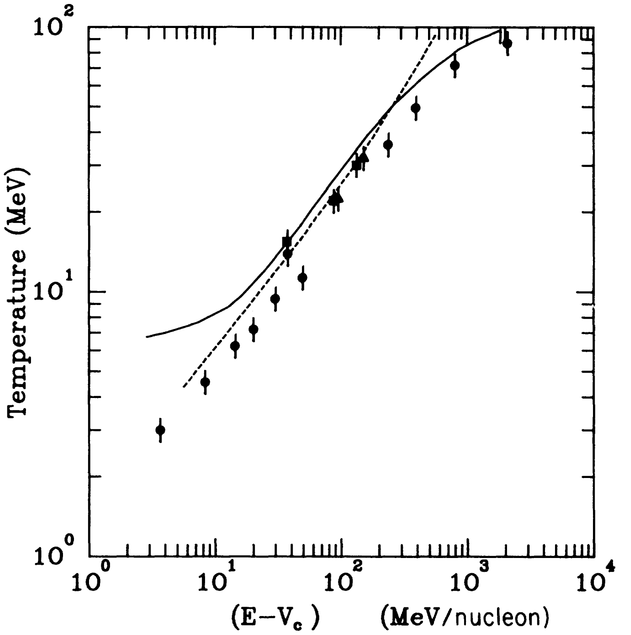

FIG. 27. Bombarding energy dependence of the temperatures extracted from the spectra of protons. Circles represent O- and Ne-induced reactions, while squares and triangles represent the present Ar- and Ne-induced reactions, respectively. The dashed line is the temperature expected from a Fermi gas model and the solid line is the prediction of the fireball model.

the theory and the data is poor, especially at forward angles where the fireball model underpredicts the high energy tails of the spectra. The comparison of the calculated and observed temperatures is best done at 90° where the transformation to the laboratory has the smallest effect. For all three particles the 90° theory and data show a very similar slope. At the most probable impact parameter for Ar + Au, $b=5.2$ fm, the temperature of the fireball is 31 MeV, compared with 30 MeV extracted from the proton spectra with the single moving source fit.

The fireball predictions reproduce the data better for relativistic collisions[5] than the results shown in Fig. 29. It is clear that the simple geometrical assumptions of the fireball model should break down for intermediate energies. Several estimates have been made for the times required for various phases of the reaction. Bertsch and Cugnon estimated that the entropy per participant nucleon decreases to a constant value (the entropy increases, but the number of struck nucleons increases faster) in about 3×10^{-23} sec.[57] At this point the participant has gained the maximum number of nucleons and begins to expand. The cooling of the hot zone has been calculated to be in the 10^{-23} sec range as well.[58] In addition, the freezeout time has been estimated at 4×10^{-23} sec by following the time development of fragment distributions and comparing to observed distributions.[59] In order to evaluate the fireball geometrical picture, these source lifetimes of approximately 5×10^{-23} sec should be compared with the transit time of a 137 MeV/nucleon Ar nucleus

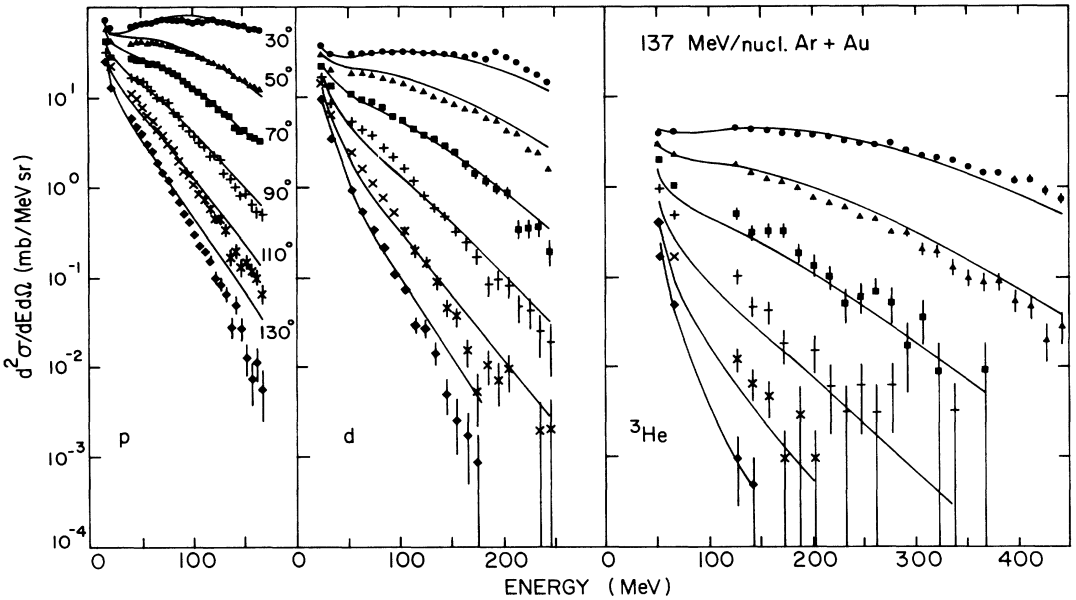

FIG. 28. Fits to the p, d, and ^{3}He spectra from 137 MeV/nucleon Ar + Au with three moving sources.

through a Au target of about 15×10^{-23} sec. It is clear that the projectile is not well separated from the target by the time the source emits particles and that the interaction of the hot, compressed matter with the surrounding spectator nucleons should be taken into account for intermediate energy collisions.

B. Coalescence model

The constancy of the temperatures extracted from the moving source fits suggest a common origin for the fragments and light particles. Formation of complex nuclei in heavy ion collisions has been described by final state interactions, or coalescence of emitted nucleons.[46,60–62] In this model, composite fragments are formed when nucleons are emitted close together in phase space. Nucleons within a specified momentum radius, p_0, are assumed to coalesce into light nuclei while the rest are emitted as free nucleons. With the assumptions that the density of nucleons is considerably less than normal nuclear density, that the proton and neutron spectra are identical in shape, and that the formation of light nuclei does not significantly deplete the original nucleon distribution, a simple scaling law is obtained where the composite fragment cross sections are obtained by raising the proton cross section to the power of the fragment mass number, A.

The scaling relationship can be expressed as[60]

$$E_A(d^3\sigma_A/dp_A^3)=C_A[E_p(d^3\sigma_p/dp_p^3)]^A\ , \qquad (7)$$

where A is the fragment mass number, $d^3\sigma_p/dp_p^3$ and $d^3\sigma_A/dp_A^3$ are the proton and complex fragment momentum space densities, respectively, at the same velocity, E_p and E_A are the proton and fragment total energies, respectively, and C_A is the scaling factor. The coalescence radius can be expressed as[60]

$$p_0^3=(3m\sigma_0/4\pi)\times\{C_A[(Z_t+Z_p)/(N_t+N_p)]^N A^2 N!Z!\}^{1/(A-1)}\ , \qquad (8)$$

where N, N_t, and N_p are the fragment, target, and projectile neutron numbers, respectively, Z, Z_t, and Z_p are the fragment, target, and projectile proton numbers, respectively, m is the nucleon rest mass, and σ_0 is the geometric reaction cross section with $r_0=1.2$ fm.

In Fig. 30 the results are shown for coalescence model fits to the deuteron spectra for Ar + Au and Ar + Ca re-

TABLE IX. Parameters for fit to 137 MeV/nucleon Ar + Au data with three moving sources. An asterisk means the parameter was held fixed during fitting.

	Projectile-like			Intermediate			Target-like		
Particle	τ (MeV)	σ_0 (mb)	β	τ (MeV)	σ_0 (mb)	β	τ (MeV)	σ_0 (mb)	β
p	8.0*	43 600*	0.51*	28.6	34 500	0.23	4.2	8100	0.02*
d	8.0*	20 000*	0.51*	32.9	18 400	0.24	8.0*	6000	0.02*
^{3}He	8.0*	3000*	0.51*	37.2	2800	0.27	6.9	7000	0.02*

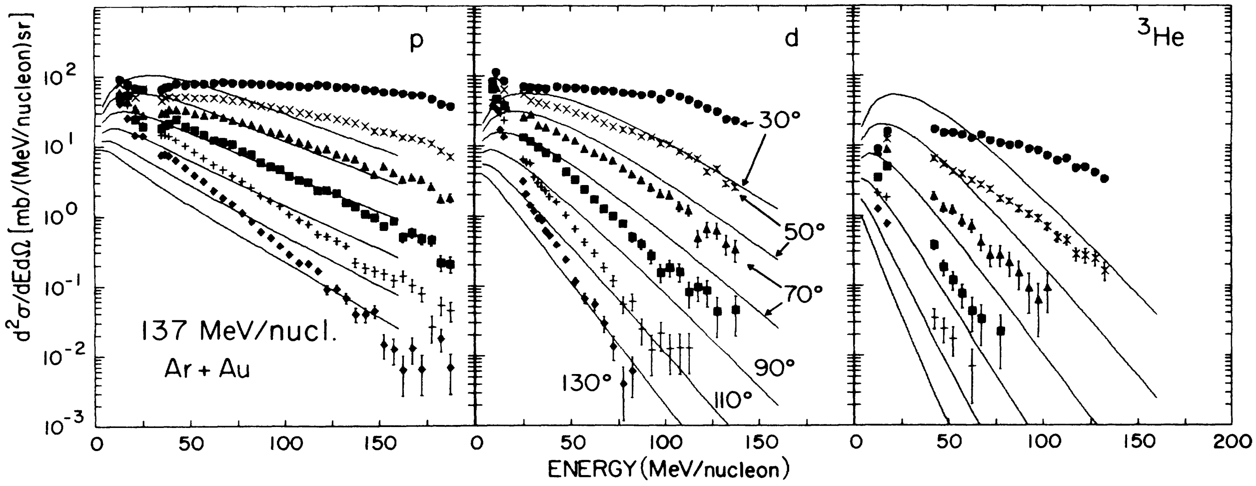

FIG. 29. Predictions of the fireball model (solid lines) and data for p, d, and ^{3}He from 137 MeV/nucleon Ar + Au.

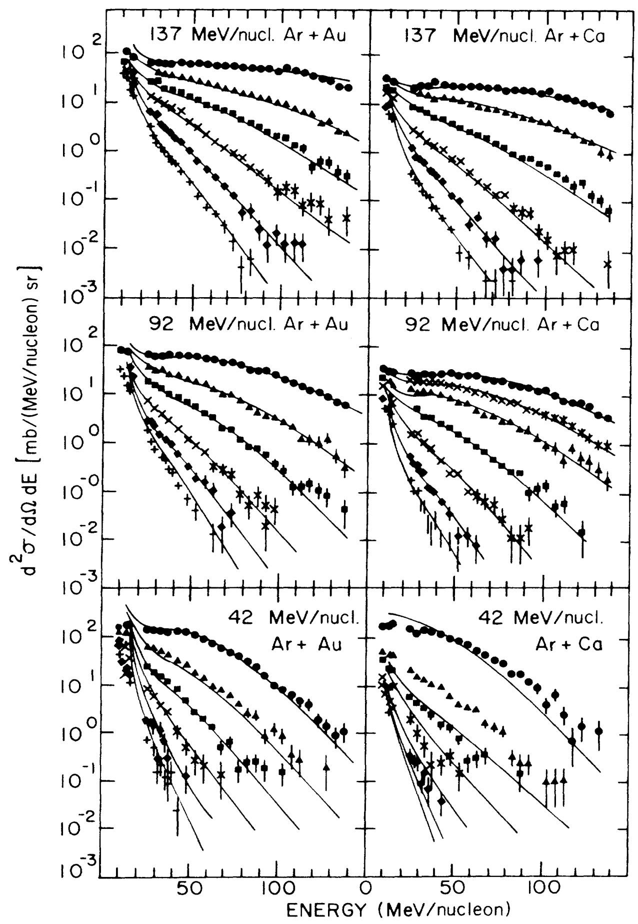

FIG. 30. Coalescence model fits to the deuteron spectra from Ar-induced reactions. The angles shown are 30°, 50°, 70°, 90°, 110°, and 130°. All angles were fitted with a single coalescence radius.

actions at 42, 92, and 137 MeV/nucleon. The solid lines represent the coalescence model and the agreement between the model and the data from the six different systems is very good. Representative energy spectra at 30° and 90° for Ar + Au are presented in Fig. 31 for fragments up to $A=14$. The angles and particles that are not shown follow the trends demonstrated by the angles and particles shown. An example of the complete angular distribution of spectra for ^{7}Be is given in Fig. 32. The solid lines in both figures represent the proton energy spectra at the same energy per nucleon in the laboratory raised to the Ath power as described above. A single normalization is used for all angles, which leads directly to the extraction of the coalescence radius for that particle from each type of reaction using Eqs. (7) and (8). The resulting coalescence radii are plotted in Fig. 33 as a function of fragment mass for two incident Ar energies, 92 and 137 MeV/nucleon, and two targets, Ca and Au.

In Fig. 33 one can see that the coalescence radii are relatively independent of the fragment mass within errors, although there is an apparent trend toward higher values above $A=8$. Statistically, the values from both energies for each target can be described by one value of the coalescence radius, $p_0=157.2$ MeV/c for Ar + Ca and 154.7 MeV/c for Ar + Au. This constancy can be interpreted as evidence that these fragments are all emitted from a common source, and it is in agreement with the result of single moving source fits.

One can relate the extracted coalescence radius to the radius of the interaction zone between the target and projectile nuclei, R, using the following formulation,

$$R^3=(Z!N!)^{1/(A-1)}(9h^3/16\pi\tilde{p}_0^3)\ , \tag{9}$$

where $\tilde{p}_0$ is the reduced coalescence radius defined as

$$\tilde{p}_0^3=(\{2^A/[A^3(2S_A+1)]\}^{1/(A-1)})p_0^3\ , \tag{10}$$

and S_A is the ground state spin of the fragment. The interaction radii are shown in Fig. 33 along with the coales-

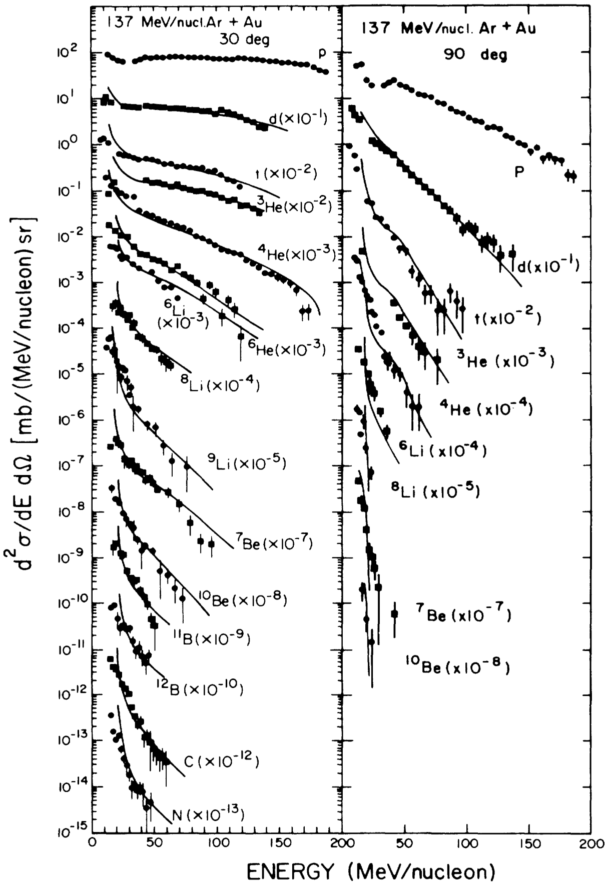

FIG. 31. Coalescence model results for fragment spectra at (a) 30° and (b) 90°.

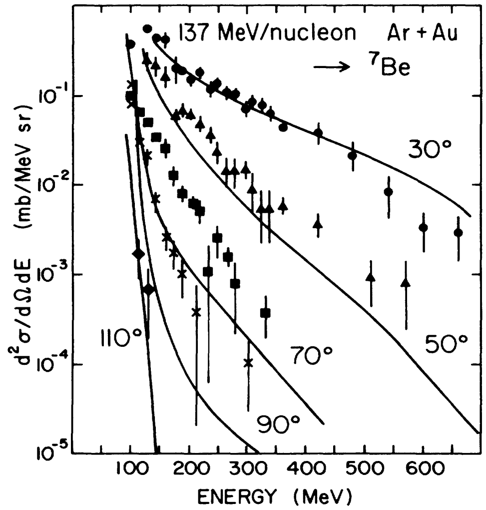

FIG. 32. Coalescence model fit to the ^{7}Be spectrum from 137 MeV/nucleon Ar + Au. The angles shown are 30°, 50°, 70°, and 90°. All angles were fitted with a single coalescence radius.

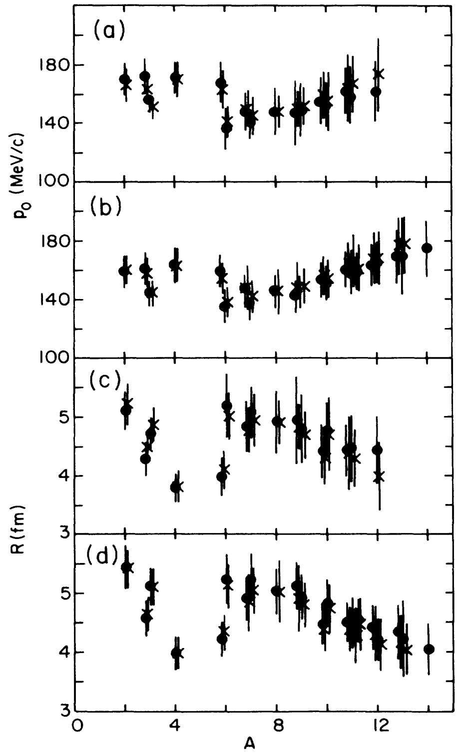

FIG. 33. The coalescence radii are given in (a) for Ar + Ca and (b) Ar + Au. The interaction zone radii are given in (c) for Ar + Ca and (d) Ar + Au. The circles and crosses represent, respectively, the cases for 137- and 90-MeV/nucleon projectile energy.

cence radii as a function of observed fragment mass number. The radii are statistically consistent with a constant value of 4.5 and 4.7 fm for Ar + Ca and Ar + Au, respectively, although the trend for the heavier fragments is toward smaller radii.

The present results for interaction volume radii agree approximately with the results[63] for 400 MeV/nucleon Nb + Nb and Ca + Ca using the Plastic Ball model. In that work the interaction volume was measured using two proton correlations as a function of the observed charged particle multiplicity. However, the observed radius was almost constant above a multiplicity of 10 with $R\approx 4$ fm for Ca + Ca and $R\approx 5$ fm for Nb + Nb. Because the present analysis deals with complex fragments emitted at intermediate rapidities, the results must be biased toward central collisions and indeed the interaction volume is similar to that found using the high multiplicity selected data in Ref. 63. Other particle correlation measurements have yielded similar interaction radii for multiplicity averaged data. A proton-proton correlation measurement[64] for 25 MeV/nucleon O + Au obtained $R\approx 5$ fm (≈ 4 fm Gaussian), while a two pion correlation measurement[65] for 1.5 GeV/nucleon Ar + KCl yielded $R = 6.0\pm 0.6$ fm (4.9 ± 0.5 fm Gaussian).

C. Deuteron-to-proton ratios and entropy

Even though the dynamics of the reaction are not as simple as assumed in the fireball model, a consistent picture emerges from thermal, TDHF, hydrodynamical,[34,66] and intranuclear cascade calculations.[39,40,57] As the nuclei interpenetrate each other, nuclear matter is compressed and highly excited. From the state of highest density $[\rho > (2-4)\rho_0]$ and temperature, the system expands at approximately constant entropy towards lower densities, $\rho \leq \rho_0/2$. During the expansion the temperature drops, and in the late stages of the reaction the system disintegrates and the finally observed fragments are formed.[55,56,57] The success of the coalescence approach further supports the idea of thermalization during the reaction.

Our goal in performing these studies was to learn about the conditions present during the hot, dense early stage of the reaction. Due to the expansion of the thermalized subsystem, however, the temperature values derived from the observed slopes do not directly reflect the actual initial temperature and we must study other properties of the system. The entropy per nucleon, S/A,[68] is a state variable which is expected to stay constant during the expansion, and hence we need to determine a measure for the entropy.

It has been suggested that if chemical equilibrium is indeed reached and the system can be described in terms of an ideal gas, the entropy can be deduced from the observed deuteron-to-proton ratio R_{dp}.[69] If the number of protons greatly exceeds the number of deuterons and if formation of other clusters as well as the deuteron binding energy can be neglected, the entropy per nucleon is[69,70]

$$S/A = 3.95 - \ln(R_{\mathrm{dp}}) . \tag{11}$$

Since, experimentally, $R_{\mathrm{tp}} \ll R_{\mathrm{dp}} < 0.4$ at $E > 400$ MeV/nucleon,[7,71] this simple formula was expected to be applicable. However, the entropy extracted from the data in this way is much larger than expected.

The experimental R_{dp} is almost constant with bombarding energy, leading to a flat energy dependence of the entropy. This behavior is inconsistent with the expected drop with decreasing bombarding energy of the entropy generated in the collision.[68] Even for incident energies greater than 400 MeV/nucleon, the values of S/A extracted from observed R_{dp} values exceed the entropies calculated in a hydrodynamical model.[66] On the other hand, the deuteron-to-proton ratios obtained from the model combined with a chemical equilibrium calculation agree well with the experimental data over the whole range of bombarding energies considered. This apparent paradox can be explained by the decay of particle-unstable excited nuclei $A^* \rightarrow (A-1)+\mathrm{p}$, which becomes increasingly important at intermediate and low bombarding energies. Hence the relation between the entropy and the observed R_{dp} is not given by the simple formula of Eq. (11).

To learn about the entropy, we must include these additional states into any equations connecting the entropy with experimentally observable quantities, requiring a much more complicated theoretical treatment. Including the decay of particle-unstable nuclei influences the experimental approach to measuring the entropy as well. Many protons are created by the decay of complex fragments with $A > 4$, a mass region not covered by many experiments. As the beam energy is lowered into the intermediate energy regime, the cross sections for heavier fragments relative to the light particle cross sections increase considerably. Thus it becomes especially important to take heavier fragments into account when studying the entropy from intermediate energy collisions.

D. Quantum statistical model

1. Description

Many statistical models have been formulated to describe the production of fragments heavier than deuterons. These models range from the sequential decay of the Hauser-Feshbach approach[25] to explosion-evaporation models incorporating classical[72,73] or quantum statistics. We have used a quantum statistical model of nucleons and nuclei in thermal and chemical equilibrium at a given temperature and density. We have extended current quantum statistical models[54,67] to take into account ground state and γ-unstable nuclei up to $A = 20$, and the known particle-unstable nuclear states up to $A = 10$. The truncation of available states makes the predictions of this model less reliable above $A = 10$. However, comparisons with data are not done above $A = 14$. The model treats fermions and bosons with the correct statistics and incorporates excluded volume effects, pions, and the Δ resonance. The model does not include dynamical aspects of the reaction. It presupposes the existence of a thermalized subsystem and requires a choice of how much expansion takes place before the fragments cease to interact. This freezeout density is typically taken as 0.3—0.5 times normal nuclear matter density ($\rho_0 = 0.17$ nucleons/fm^3). Recently, this freeze-out density has been estimated at $0.25\rho_0$ by a measurement of correlated particles as a function of multiplicity.[63]

2. Calculated deuteron-to-proton ratios

Figure 34 shows the deuteron-to-proton ratio obtained from the quantum statistical calculation. The curves are labeled by the point particle densities, $\rho_{\mathrm{pt}}/\rho_0 = 0.5$ and 0.1, corresponding to breakup densities $\rho_{\mathrm{bu}}/\rho_0 \approx 0.32$ and 0.09, respectively. The value of R_{dp} in chemical equilibrium is given by the curve labeled $R_{\mathrm{dp}}^{\mathrm{primordial}}$. In contrast to expectations from the data, R_{dp} is not much smaller than unity, but, in fact, approaches unity at $S/A \approx 2$. Due to the decay of the particle-unstable nuclides, $R_{\mathrm{dp}}^{\mathrm{final}}$ drops substantially. It is noteworthy that $R_{\mathrm{dp}}^{\mathrm{final}}$ is nearly independent of the exact value of the breakup density,[66] and $S(R_{\mathrm{dp}})$ varies by about 10% despite variations in the point-particle densities of a factor of 5.

Also evident from Fig. 34 is the fact that R_{dp} is a multivalued function of the entropy. The triton and ^{3}He to proton ratios are also multivalued functions of S/A, and may carry information about the entropy for high or low incident energies, but not for intermediate energy collisions.

The independence of the ratios on the breakup density eliminates the only unknown parameter, ρ_{bu}, from the calculation. The extracted entropy per nucleon, however, depends on whether the matter from which the fragments are formed has actually participated in the violent interac-

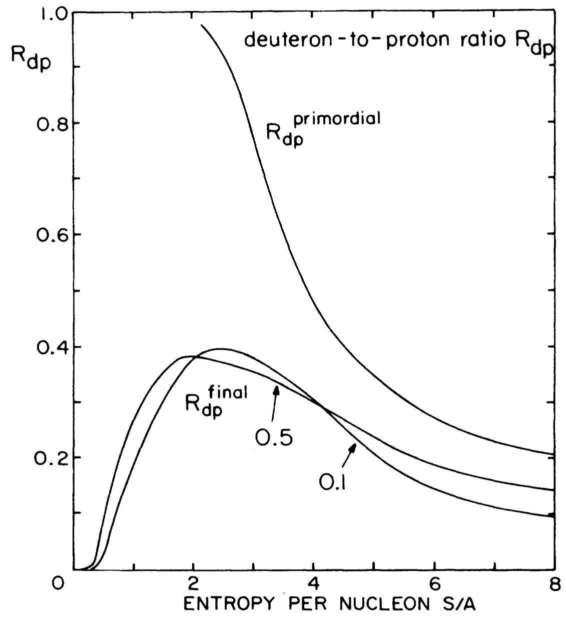

FIG. 34. Deuteron-to-proton ratios calculated from the quantum statistical model at two breakup densities, $\rho=0.1\rho_0$, and $0.5\rho_0$. The primordial and final (after decay of excited states) ratios are shown.

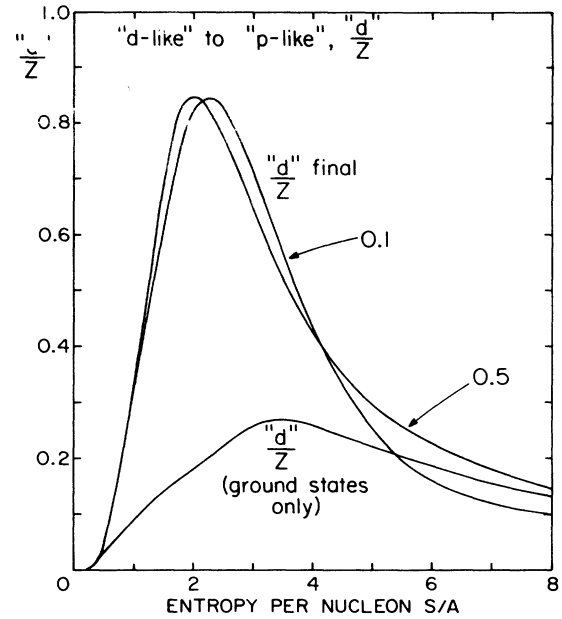

FIG. 35. Ratio of deuteron-like to proton-like particles from the quantum statistical model at two breakup densities, as in Fig. 34. The primordial $R_{\text{"d"}Z}$ includes only the ground states of nuclei with $2 \leqq A \leqq 4$.

tion or whether it has been a projectile or target spectator. Therefore, we expect a distribution of entropy values in coordinate as well as in momentum space even in a single collision (i.e. the mean entropies of the participant matter, the projectile-like fragments and the target-like fragments). Since R_{dp}, R_{tp} and $R_{^3\text{He}p}$ reach plateaus in the intermediate energy regime, we need a different messenger to provide information on the entropy.

It has been suggested[57,74] that the entropy may be studied via $R_{\text{"d"}Z}$, the ratio of deuteron-like to proton-like particles. This ratio is expressed in terms of the number of observed correlated nucleon pairs in light clusters $[1\times d+3/2(t+{}^3\text{He})+3\times{}^4\text{He}]$ divided by the total number of observed protons (including bound protons). This approach takes into account formation of clusters heavier than deuterons, but neglects particle-unstable clusters. Figure 35 shows the primordial $R_{\text{"d"}Z}$, which includes only the ground states of the nuclides $2\leqq A\leqq 4$, and the finally observable $R_{\text{"d"}Z}$, which also includes the decay products as a function of the entropy. The behavior is qualitatively the same as for R_{dp}. The value of $R^{\text{final}}_{\text{"d"}Z}$ is strongly affected by the decay of excited clusters and shows a maximum at $S/A\approx 2$.

E. Entropy extracted from fragment distributions

We can use the quantum statistical model to learn about the entropy using measured mass distributions including heavy fragments. The entropy is extracted by performing the calculation at a given S/A and density ρ, thus fixing the temperature. The density used corresponds to the breakup density, where the emitted particles no longer interact. A density of $0.5\rho_0$ was used for these calculations, but the fragment distributions are not very sensitive to the assumed breakup density for $0.3\rho_0<\rho<0.8\rho_0$.[47] The N and Z of the initial system are chosen to be those of the fireball at the most probable impact parameter. The entropy is then determined by a least-squares fit of the calculated yields to the observed fragment distributions. It should be noted that in the calculation excited states are populated and then decay only via their normal decay channels, which implies that excited fragments decay only after freeze-out has occurred. Recent experiments[75] have shown that final state interactions are present that cause the observed distribution to be somewhat different from the distribution resulting from the ground plus decayed excited states.

1. Intermediate rapidity fragments

The top part of Fig. 36 shows the measured mass distributions for the Ar + Au reactions. The solid histograms show the results of the best fit with the quantum statistical model. The lower part of the figure shows the entropy values obtained from the fits: $S/A=2.0\pm0.2$, 2.2 ± 0.2, and 2.35 ± 0.2 for $E_{\text{lab}}=42$, 92, and 137 MeV/nucleon, respectively. The solid line shows the average entropy per nucleon expected for the participants using a conventional hydrodynamic calculation, and the dashed line the result for a viscous fluid.[68] Entropies in the range of 4—6 were previously extracted from the observed deuteron-to-proton ratios. The present entropy values are lower than these, but still higher than those expected from hydrodynamical calculations.[47] It should be noted that the theoretical results correspond to an upper limit for the entropy produced, because in the calculation the incident matter stops. At low energies the mean free path of the nucleons may be quite long, causing the nuclei be rather transparent to one another and little or no entropy to be produced in the collision.

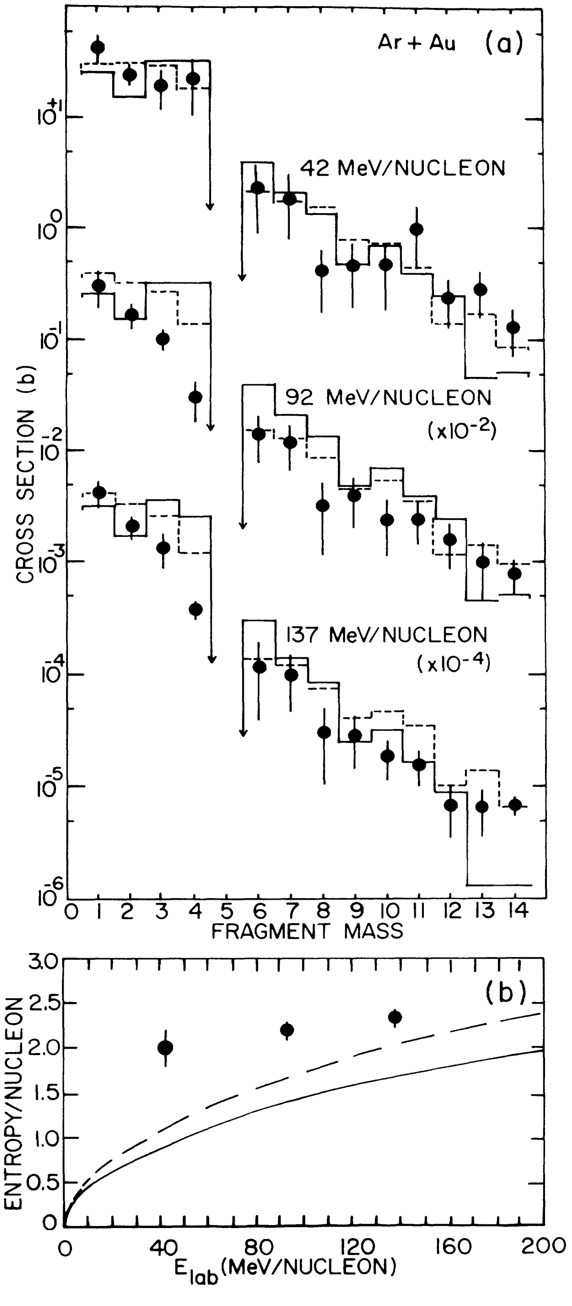

FIG. 36. (a) Fragment production cross sections. The solid and dashed histograms are results of quantum statistical and Hauser-Feshbach calculations, respectively. (b) Entropy extracted from the fits, as a function of bombarding energy. The solid and dashed lines are the entropies expected from nonviscous and viscous fluids.

To determine the extent to which the extracted entropy depends on the assumed breakup mechanism, we have performed a calculation based on the Hauser-Feshbach formalism.[25] These results are shown in the top of Fig. 36 as the dashed histograms. In this approach, particles are statistically emitted from an excited nucleus at constant density, and the temperature, charge, and mass evolution of the system are followed. Emission of nuclei in ground and particle-stable excited states as well as unstable states with lifetimes long compared to the emission time is included. A spherical initial system with $Z=34$ and $A=82$ was assumed, again corresponding to the fireball at the most probable impact parameter. The entropy extracted is for the initial system with a level density corresponding to an ideal Fermi gas. Entropies determined by fitting the measured mass yields with respect to temperature at fixed Fermi energy ϵ_F were found to be rather independent of ϵ_F in the range $24<\epsilon_F<60$ MeV. The histograms represent calculations for $\epsilon_F=38$ MeV, corresponding to an ideal Fermi gas at normal nuclear matter density.

The entropy values deduced from the two very different approaches to the dynamics of the reaction, the explosion picture of the quantum statistical model and the sequential emission of the Hauser-Feshbach model, are consistent to within S/A of 0.2. This agreement confirms the independence of the entropy determination from assumptions about the breakup dynamics.

2. *Rapidity dependence of the entropy*

This work is one of the few studies of fragments heavier than alpha particles emitted from the participant region of the reaction. However, a large body of data exists on the emission of target rapidity fragments from proton- and heavy-ion-induced reactions on heavy targets. We can apply the method described above to study the bombarding energy dependence of the entropy produced in the target remnant, and to investigate the differences in the entropy produced in the participant and spectator regions of the reaction.[76]

In Fig. 37 relative production cross sections are shown for target rapidity fragments from the reactions of 400 MeV/nucleon Ne + U,[5] 2.1 GeV/nucleon Ne + Au,[21] 480 MeV p + Ag,[77] and 80–350 GeV p + Xe.[78] The solid lines in the figure represent the quantum statistical calculation described above carried out at a density of $\rho=0.3\rho_0$. Although data were measured up to $A=30$ for the p + Xe case, only the cross sections that can be compared with the present model are shown. The fits agree well with the observed fragment yields for all four cases, except for $Z=2$ fragments from 480 MeV p + Ag.

The entropies obtained from the fits to these fragment distributions as well as those extracted from the reactions of 30 MeV/nucleon C + Au,[79] 55–110 MeV/nucleon C + Ag,[80] 250 MeV/nucleon Ne + Au,[21] 2.1 GeV/nucleon Ne + U,[5] and 4.9 GeV p + Ag and U (Ref. 81) are shown in the top of Fig. 38 as a function of the incident energy. The depicted errors reflect the errors from the fits as well as known systematic errors in the data. The fits generally encompass fragments with $3\leq Z\leq 10$ and appear to be independent of both projectile type and

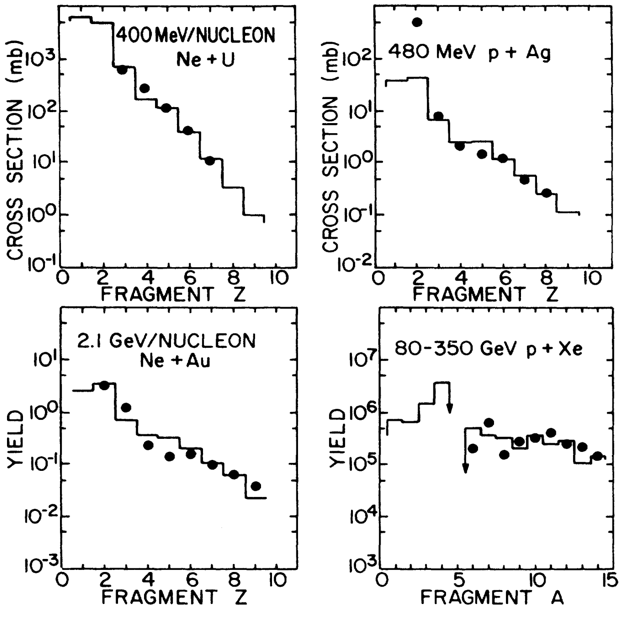

FIG. 37. Mass distributions of target rapidity fragments. The histograms are fits with the quantum statistical model.

energy. The average value for S/A in these cases is 1.84 ± 0.16. Not shown in this figure is S/A extracted from 80–350 GeV p + Xe,[78] which is 1.46 ± 0.67. This constant value of about 1.8 for the extracted S/A coincides with the expected entropy of nucleons in the target nucleus if it is excited to its binding energy, and suggests that there is a limit to the amount of energy the target remnant is able to absorb from the projectile and/or participant region before it breaks up.[76]

The open squares in the lower section of Fig. 38 show the extracted entropies for the intermediate rapidity fragments from the Ar + Au reaction. These values are higher than those extracted from target fragments and increase slightly with bombarding energy. No complex fragment data currently exist at energies above 137 MeV/nucleon, as the data of Refs. 5 and 21 do not extend to intermediate rapidities for the heavier fragments. We are therefore unable to follow the energy dependence of the entropy over a large range of bombarding energies. The figure contains S/A values expected from a fireball model taking into account the slowing from Coulomb repulsion between the two nuclei and calculating the entropy using the Fermi gas model. These calculations are shown as solid lines for three densities, $\rho = 1.0\rho_0$, $2.0\rho_0$, and $3.0\rho_0$. The maximum density of the fireball should increase with beam energy, so these curves are clearly a

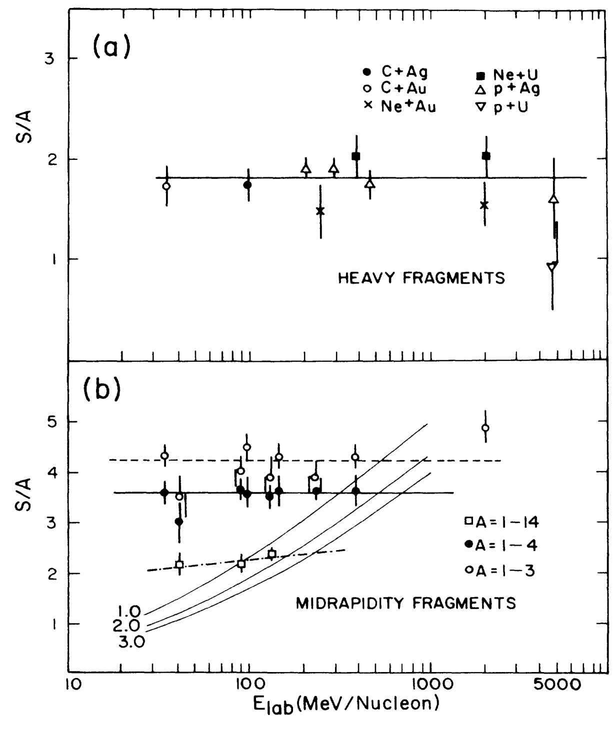

FIG. 38. Extracted entropy per nucleon: (a) from target rapidity fragments, and (b) from midrapidity fragments. The solid and dashed lines represent the weighted average for fragments with $1 \leq A \leq 3$ and $1 \leq A \leq 4$, respectively. The three grouped solid lines show the entropy calculated using a fireball geometry and a Fermi gas model at three different values of ρ/ρ_0.

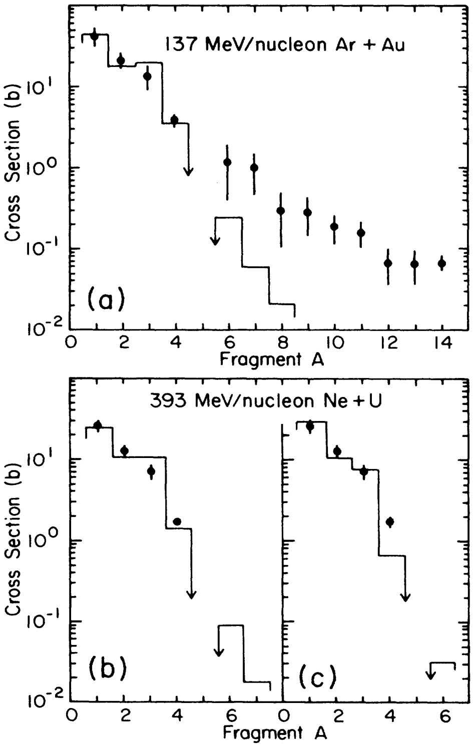

FIG. 39. Intermediate rapidity fragment distributions, and quantum statistical model results. In (a) and (b) fragments with $1 \leq A \leq 4$ are fitted, while in (c) only fragments with $1 \leq A \leq 3$ are fitted.

rough estimate of the expected behavior of the entropy.

The extracted entropies from intermediate rapidity fragments with $1 \leqq A \leqq 3$ and $1 \leqq A \leqq 4$ from nucleus-nucleus reactions are also shown in the bottom of Fig. 38. Typical fits to intermediate rapidity light particles only are shown in Fig. 39. In the top of the figure, light fragments with $1 \leqq A \leqq 4$ from 137 MeV/nucleon Ar + Au are fitted, while fragments with $1 \leqq A \leqq 4$ and $1 \leqq A \leqq 3$ from 393 MeV/nucleon Ne + U (Ref. 6) are fitted in the left and right lower sections, respectively. In addition to the results from this work, included in Fig. 38 are 35 MeV/nucleon C + Au,[19] 241 and 393 MeV/nucleon Ne + U,[6] and 2.1 GeV/nucleon Ne + Pb.[7] The average value of S/A for fragments with $1 \leqq A \leqq 3$ and $1 \leqq A \leqq 4$ are 4.24 ± 0.32 and 3.60 ± 0.12, respectively, independent of the incident energy and projectile nucleus. These values can be compared to the entropies extracted from the deuteron to proton ratios, where $S/A = 4.7$ was deduced.

The difference between the entropy extracted using the same quantum statistical model compared to $1 \leqq A \leqq 4$ and $1 \leqq A \leqq 14$ cross sections is puzzling because these fragments seem to have common origins. The apparent temperatures of these fragments are similar to each other at a given bombarding energy, while the extracted source velocities vary from 0.5 times the projectile velocity for $A \leqq 3$ to 0.3 times the projectile velocity for the heavier fragments. Light particle inclusive data include contributions from more peripheral collisions, where the small number of nucleons contained in the interaction volume between the two nuclei excludes the formation of heavy fragments. The macrocanonical approach inherent in the quantum statistical model requires many particles in the system and is inappropriate for peripheral collisions. In contrast, the thermodynamic limit is approached for near-central collisions, which is where the heavier fragments are produced.[21] In fact, even when only light particles were used to extract S/A, the entropy was found to be lower when central collisions were selected.[82] This dependence provides further evidence that to learn about S/A from intermediate energy nucleus-nucleus reactions, it is necessary to include complex fragments as well as light particles.

VI. VLASOV-UEHLING-UHLENBECK MODEL AND HYDRODYNAMICS

A. Boltzmann equation

A microscopic description of high energy proton-nucleus and nucleus-nucleus collisions has been provided by intranuclear cascade calculations.[36–42] In this approach, nuclei are approximated by a collection of point nucleons. Initial nuclei with the proper sizes and Fermi momenta are constructed by giving each particle a random position and momentum vector. The reactions are treated as a superposition of independent collisions of the point nucleons, which move on straight line trajectories until they collide. The collision probability is given by the free nucleon-nucleon scattering cross sections.

The time evolution of the system is followed until the collisions cease. The quantum mechanical nature of the problem is recovered by averaging the final result over many ensembles with different initial nucleon positions and momenta, and different random choices for the outcomes of the two-nucleon collisions.

The intranuclear cascade may be viewed[41] as an approximate solution of the Boltzmann equation. The Boltzmann equation is a kinetic equation for a dilute gas of classical point particles interacting through a potential,[83] and includes both mean field and collision terms. In the limit of relativistic nuclear reactions, the classical collision term dominates the single particle distribution and so the mean field term is omitted in intranuclear cascade calculations.

In order to apply the Boltzmann equation for intermediate energy reactions, we must take the mean field term into account, and replace the classical collision integral by the Uehling-Uhlenbeck collision terms,[84] which respect the Pauli principle. The equation describing the single particle distribution function f is then given by[85,86,43]

$$\frac{\partial}{\partial t}f + \mathbf{v}\cdot\frac{\partial}{\partial \mathbf{r}}f + \mathbf{a}\cdot\frac{\partial}{\partial \mathbf{v}}f = \frac{d^3p_2\,d^3p_1'\,d^3p_2'}{(2\pi)^6}\sigma v_{12}[ff_2(1-f_1)(1-f_2)-f_1f_2(1-f)(1-f_2)]\delta^3(p+p_2-p_1'-p_2') \; . \tag{12}$$

Equation (12) shows that the time evolution of f is due to two distinct causes: the free motion of the particles and the two-body collisions. The potential field keeps the nuclei from expanding before collisions occur. The motion of the test particles under the influence of this field alone is governed by the left hand side of Eq. (12) set to zero. This equation is the Vlasov equation, which could be used to simulate collisions at very low bombarding energies.

In the following sections we review the implementation of the additional terms into the Monte Carlo framework provided by the intranuclear cascade approach. Our calculation follows the method of Cugnon[87] and extensions made in Ref. 43.

1. *Nucleon-nucleon cross sections*

Our goal was to produce a generally applicable microscopic theory which could be used for asymmetric as well as symmetric systems. We have therefore incorporated protons, neutrons, deltas, and pions of different isospin separately with their experimentally determined scattering cross sections. Because we wish to carry out calculations for projectile energies as low as 40 MeV/nucleon, we have extended the tabulated scattering cross sections in our code to include the correct details for collisions at low energies. The calculation includes production of pions directly and through deltas, and also the pion absorption cross sections as determined from detailed balance.[40]

2. *Pauli blocking*

The Pauli blocking factor for each particle is given by $(1-f)$, and the scattering cross section is then reduced by the Uehling-Uhlenbeck factor $(1-f_1)(1-f_2)$.[43] To allow calculation of f, a six dimensional sphere containing N nucleons in the initial system (i.e., at normal nuclear matter density) is defined,

$$N=\frac{4}{(2\pi\hbar)^3}\frac{4}{3}\pi\tilde{r}^3\frac{4}{3}\pi\tilde{p}^3 ,$$

where $\tilde{r}$ and $\tilde{p}$ are radii in configuration and momentum space, respectively. In this work $N=4$ particles was used. The value of N is the result of a compromise between the need for small radii to ensure a uniform local density and the need for large N to reduce statistical errors in counting the nucleons in the sphere.

Once the phase space coordinates of the scattered particles are determined, the particle density in the six dimensional sphere is computed. In order to decrease the statistical error in this density, we use an ensemble averaged density, requiring simulation of 15 collisions simultaneously. The number of particles in the sphere is compared to the four particles expected in normal nuclear matter; the ratio of these two numbers gives the occupation (or blocking factor) f, and the collision probability factor $(1-f)$. When the particle is near a surface of the system, the test sphere is calculated, removing a pole cap with the unoccupied volume. With this correction, the Pauli blocking was 96% efficient.

Upon incorporating this Pauli blocking mechanism, we found that a large fraction of the attempted collisions was blocked for reactions at low bombarding energies. In the Ar + Ca system, 80% of collisions at 137 MeV/nucleon, 83% of collisions at 92 MeV/nucleon, and 90% of the attempted collisions at 42 MeV/nucleon were blocked.

3. *Mean field term*

A constant time-step integration routine is used to ensure synchronization of the ensembles.[43,45] The acceleration of the particles in the field is calculated at the beginning of each time step and is recalculated for colliding particles prior to further transport. The local gradients of the field are computed via the difference between particle densities in hemispheres of radius 2 fm, centered around each test particle. Ensemble averaging results in a reasonably smooth single particle distribution function with about 10% fluctuations at normal density.

The density dependent potential field $U(\rho)$ is given by a local Skyrme interaction:

$$U(\rho)=-124\rho/\rho_0+70.5+(\rho/\rho_0)^2 \text{ MeV} , \tag{13}$$

with a compressibility coefficient of $K=375$ MeV.

4. *Generalized coalescence*

After the collisions among the nucleons have ceased, the resulting positions and momenta must be sorted into particle spectra to compare with experimental data. As the calculation yields only information for individual nucleons, a method to discern light nuclear clusters or large spectator fragments from single nucleons must be employed. This treatment is especially important for intermediate energy collisions where the cross sections for formation of complex fragments are quite large.[22] We have used a generalized six-dimensional coalescence approach to identify the nucleons bound in clusters.

As the two-nucleon force is short ranged, it should become negligible at a distance greater than about 3 fm. If we define a cluster as a collection of nucleons interacting with one another, but not with the rest of the system, we can conclude that a nucleon belongs to a cluster only if it is closer than a given distance r_0 to some nucleon in the cluster. Clusters formed in this manner can, however, be excited. In an excited fragment those nucleons with momenta larger than some escape momentum will be emitted from the fragment. We therefore require that nucleons within a cluster do not have momenta which differ by more than p_0 from the cluster momentum.

The algorithm has been tested on initial collision configurations, where we should find two clusters—the projectile and the target. These tests indicated that reasonable values should be around 2—3 fm for r_0, and 200—300 MeV/c for p_0. The values for p_0 are somewhat larger than those derived by applying a momentum-space-only coalescence model fit to complex particle spectra.

To perform the coalescence, we first collect all the nucleons into clusters in configuration space. We then randomly choose a particle within each cluster, and add the other particles to it if their relative momentum does not exceed p_0, recalculating the cluster momentum as nucleons are added. The parameters $r_0=2.2$ fm and $p_0=200$ MeV/c have been chosen, as they yield correct total cross sections for the observed protons.

5. *Results of the calculation for intermediate energy data*

The code resulting from the changes described above has been tested by comparisons to high energy data. Proton spectra from 800 MeV p + C reactions are reasonably reproduced. The calculation resulted in correct predictions of the pion multiplicity for relativistic Ar + KCl reactions, and the event shapes for 400 MeV/nucleon Nb + Nb collisions were found to agree with measurements.[45]

We have performed calculations for the measured Ar + Ca reactions. The calculated neutron and proton distributions were essentially identical and were combined to decrease the statistical error in the double differential proton spectra.

The upper section of Fig. 40 shows the comparison between calculated and measured proton spectra for 137 MeV/nucleon Ar + Ca at six laboratory angles between 30° and 130°. The calculated spectra agree rather well with the data, with the exception of high energy protons at 50° and 70°, which are underpredicted by a factor of 2. The same effect was found in a traditional intranuclear cascade approach applied to collisions at 1 GeV/nucleon,[42] where it was suggested that hydrodynamics may play a major role. The lower section of Fig. 40 shows the same data compared to proton spectra from the intranuclear cascade model of Cugnon,[39] which serves as a useful reference to demonstrate the importance of the mean field and Pauli blocking for intermediate energies. The resulting nucleon momentum distributions were analyzed via the same procedure as the Boltzmann equation results, including the coalescence step. It is important to note that the same coalescence parameters were used for both sections of Fig. 40. It is clear from the figure that the simple cascade simulation, though appropriate for high energies, cannot reproduce the intermediate energy data.

Figure 41 compares the Boltzmann equation calculation including the coalescence step with the data for Ar + Ca at 92 and 42 MeV/nucleon in the top and bottom sections, respectively. The coalescence parameters used were the same as at the higher energy. At 92 MeV/nucleon the calculations agree with the data and the spectra at 50° and 70° are reproduced better than at the higher bombarding energy. The calculation at 42 MeV/nucleon agrees well

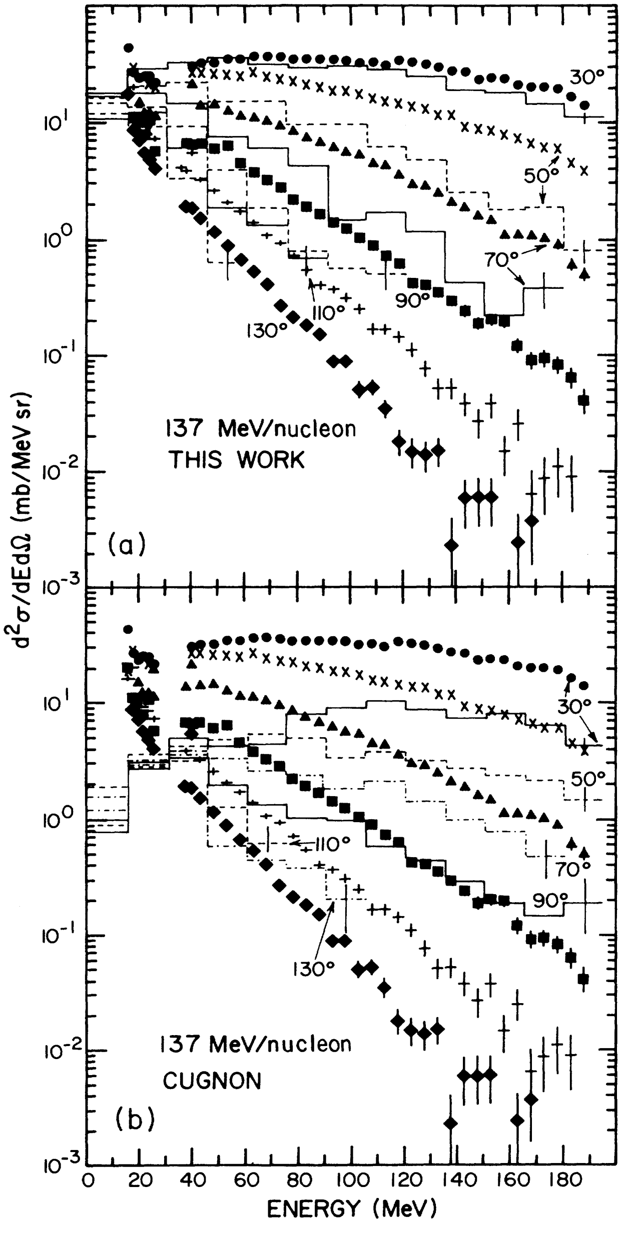

FIG. 40. Inclusive proton spectra for 137 MeV/nucleon Ar + Ca. The data are indicated by the points. (a) The histograms show results of the Boltzmann equation calculation. (b) The histograms are results obtained with the cascade model.

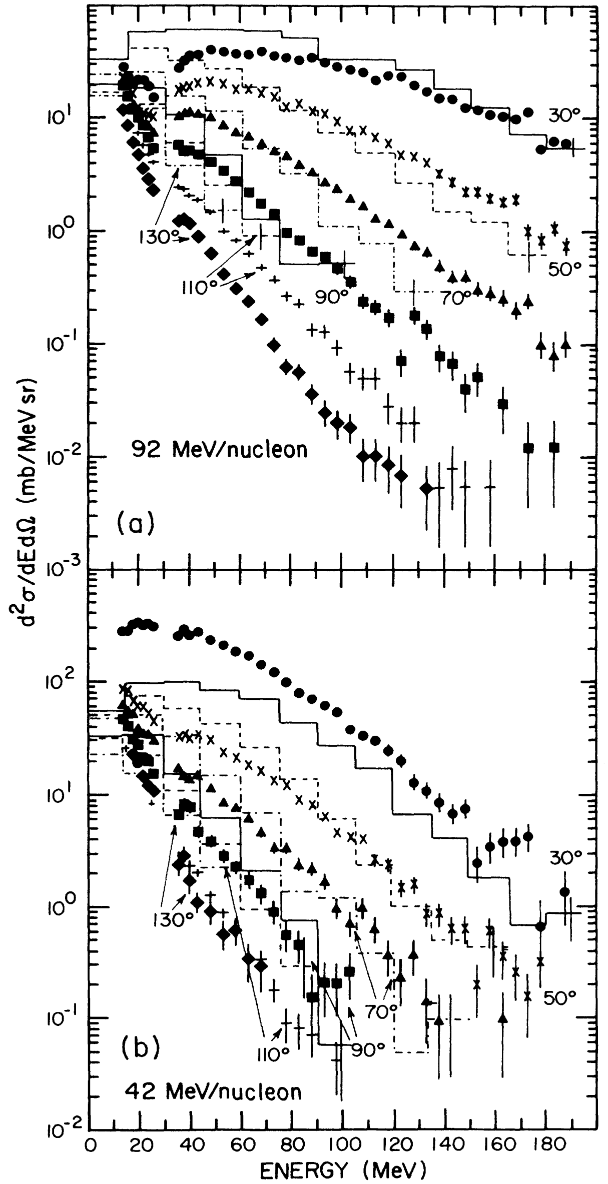

FIG. 41. The Boltzmann equation calculation is compared to the proton spectra for (a) 92 MeV/nucleon Ar + Ca and (b) 42 MeV/nucleon Ar + Ca.

with the data, except at 30°, where low energy protons are underpredicted. This disagreement is probably due to the neglect of proton evaporation from the clusters, which would dominate the projectile and target rapidity region. It is evident from these comparisons that the Boltzmann equation, including the nuclear mean field and Pauli blocking corrections to the collision terms, provides a useful calculational approach to the dynamics of intermediate energy heavy ion collisions. We can use this model to study the effect of the collision term on the mean field dynamics, as the calculation may be used in the one extreme to mimic TDHF, and on the other hand to simulate a high energy intranuclear cascade model.

B. Fluid dynamics

1. Description

The hydrodynamical calculations presented here treat the nuclear matter as a viscous fluid in three dimensions. The calculation is carried out using a grid 0.5 fm on side. For each grid element the classical fluid dynamical equations are integrated including shear and bulk viscosity and heat conductivity.[88] The nuclear binding is treated via Coulomb and Yukawa potentials.[48]

The energy of the nucleons in the system is divided into kinetic and internal energy. The internal energy is expressed in terms of the thermal energy and the compressional energy. A compressibility of 200 MeV was used and the binding energy was taken to be -16 MeV/nucleon. In the late stages of the reaction the system breaks up into nucleons and light nuclei. Thus the calculation is carried out to a density of half normal nuclear density where the assumption is made that the nucleons and nuclei cease interacting. The distribution functions and the concentrations of light nuclei up to ^{4}He are then calculated using a simplified quantum statistical model. This model is similar to the one described above except that only bound states up to $A=4$ are included.

2. Comparisons with data

Calculations were performed for 137, 92, and 42 MeV/nucleon Ar + Au reactions. The results are shown

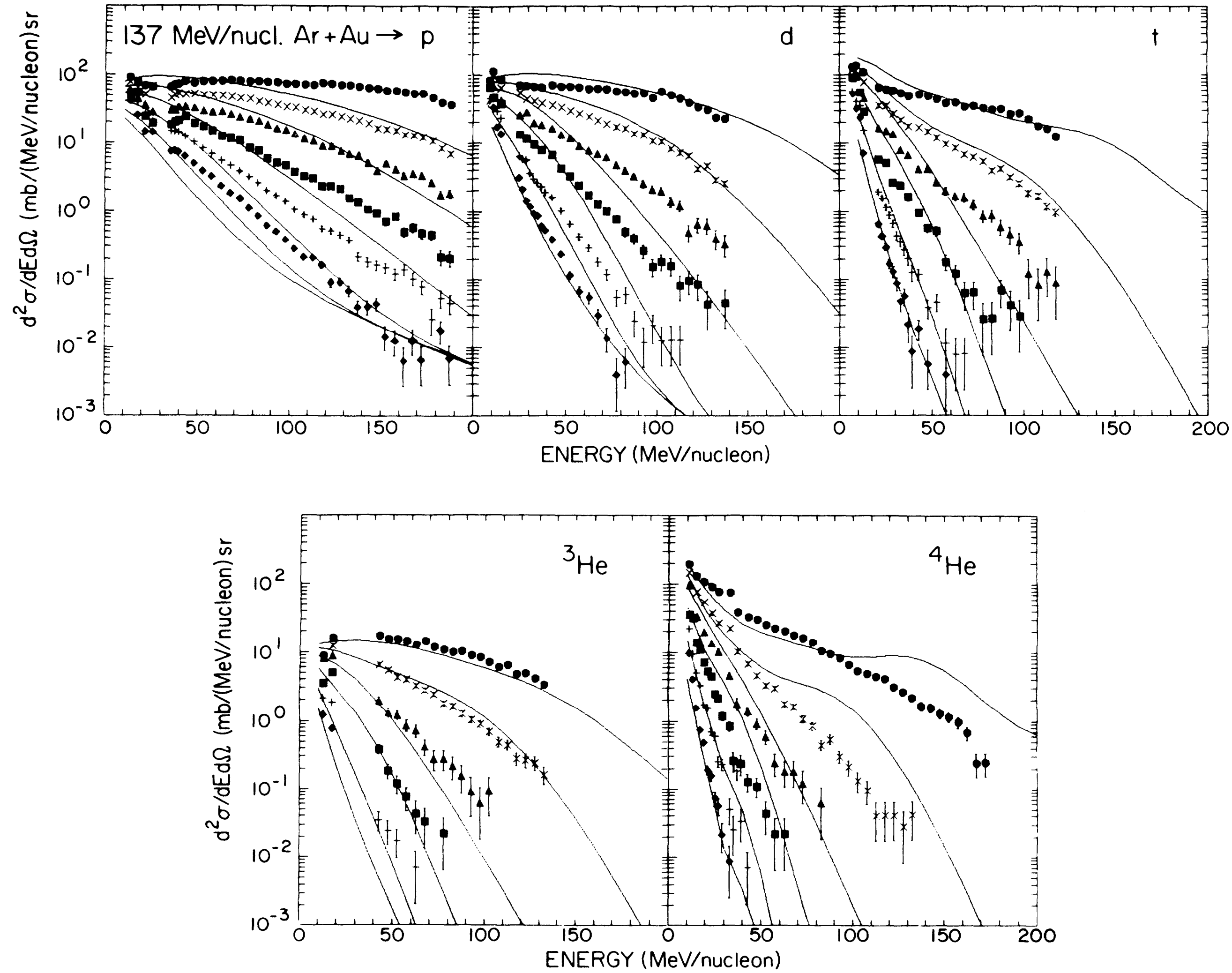

FIG. 42. Fluid dynamical results (solid lines) for light particle spectra from 137 MeV/nucleon Ar + Au.

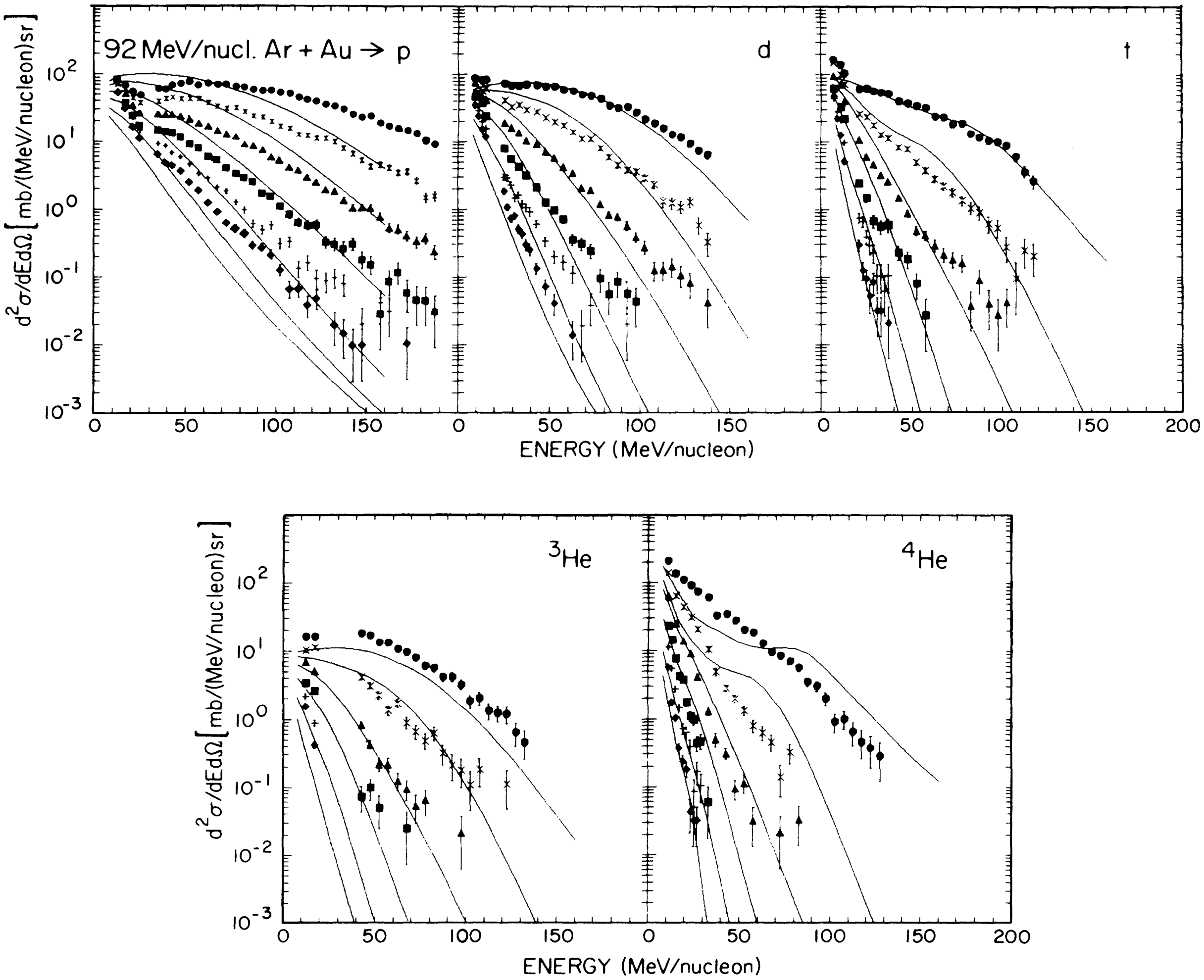

FIG. 43. Fluid dynamical results (solid lines) for light particle spectra from 92 MeV/nucleon Ar + Au.

in Figs. 42—44 normalized to the measurements using the factors given in Table X. These factors arise mainly from the simplified quantum statistical model used to calculate the relative production of the various fragments.[89] The calculation reproduces the shape of the data at 137 and 92 MeV/nucleon. The agreement is worse at 42 MeV/nucleon, indicating that the dynamics of the collision are not well described. The assumptions of the fluid dynamical model are apparently less justified at the low incident energy.

TABLE X. Renormalization factors for comparison of fluid dynamical results to light particle data for Ar + Au reactions.

Particle	137 MeV/nucleon	92 MeV/nucleon	42 MeV/nucleon
p	10	16	40
d	4	4	9
t	0.5	0.3	0.7
^{3}He	1	1	4
^{4}He	0.17	0.1	0.7

VII. SUMMARY AND CONCLUSIONS

A. Summary of results

The emission of light and complex fragments up to $A = 14$ has been studied in intermediate energy Ar- and Ne-induced reactions. The energy spectra were observed to fall approximately exponentially with energy, and could be described by a Boltzmann distribution. Plotting contours of constant cross section in the rapidity versus perpendicular momentum plane revealed that many of the observed particles arise from a source moving with a rapidity intermediate between that of the target and of the projectile. Combining this observation with the thermal appearance of the energy spectra, a subset of the data was fitted with a model that incorporates emission from a single moving source. The parameters describing the intermediate rapidity source were extracted. Fitting the full data with three sources, including a projectile-like, target-like, and intermediate sources, yielded similar values for the parameters describing the intermediate rapidity source.

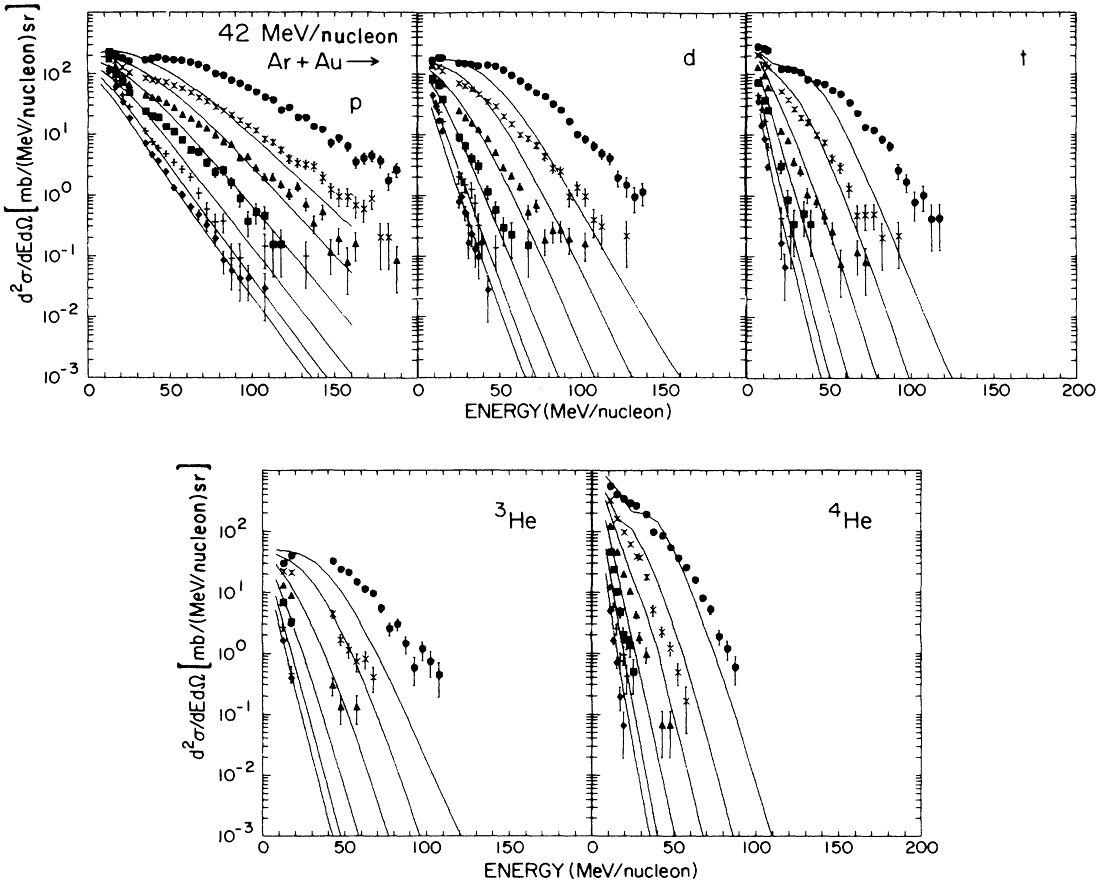

FIG. 44. Fluid dynamical results (solid lines) for light particle spectra from 42 MeV/nucleon Ar + Au.

The systematics of the extracted source temperatures and velocities were studied for various beam-target combinations. The extracted source parameters were found to be relatively independent of the mass of the emitted fragment, suggesting that complex fragments as well as light particles are emitted from a thermalized subsystem of the projectile and target.

Calculations were performed with the fireball model and the temperatures of the particle spectra were approximately reproduced, but the fireball velocity differed from the velocity of the intermediate source. This difference suggested that although the fireball geometry is inadequate at these bombarding energies, thermalization of a subset of the nucleons is still a useful concept. The question of the entropy in this thermalized system was explored, and it was shown that a quantum statistical model incorporating production of heavier fragments must be used to extract reliable information about the entropy from the data. A calculation assuming chemical equilibrium at the entropy per nucleon describing the heavy fragment ($A > 4$) distribution was unable to match the observed cross sections for light particles. However, it was recognized that the inclusive data are, in fact, summed over impact parameter and include collisions producing very small interaction regions which produce predominantly light particles. The entropy extracted from target-like fragments was found to be independent of the projectile energy and corresponded to the entropy expected for a heavy nucleus excited to its binding energy. The entropy extracted from midrapidity fragments was higher than the target rapidity data and increased with increasing bombarding energy.

The spectra of complex fragments were well described by the proton spectra raised to the Ath power. The concept of coalescence of nucleons emitted close together in momentum space into complex fragments was invoked to explain this phenomenon, and the radius of a coalescence sphere in momentum space was extracted for each observed fragment. This approach worked well for emission of fragments as heavy as nitrogen, and the coalescence radius was linked to the size of the source emitting the particles. This source was found to have a radius around 4.6 fm, in agreement with experiments measuring two-proton correlations.

The light particle data were also used to test two models describing the dynamics of the collisions. The first was a solution of the Boltzmann equation, incorporating a mean field and Pauli blocking as well as two-nucleon collisions into an extension of the intranuclear cascade approach. A generalized coalescence in phase space was used to separate the projectile and target remnants from the observed particle spectra as well as to provide predictions for spectra of light nuclei. The mean field and Pauli blocking were found to be necessary to describe the observed proton spectra.

In order to further test the limits of applicability of models describing relativistic heavy ion collisions, nuclear fluid dynamical calculations were performed. After renormalization of the calculation to the data, the agreement with light particle spectra was fair at the two higher energies, but the calculated spectral shapes were different from the observed energy distributions at 42 MeV/nucleon.

B. Conclusions

This survey of intermediate energy heavy ion reactions has answered a number of questions about the evolution of the reaction mechanism as the bombarding energy increases, but has raised many more. The concept of statistical emission from a subsystem of the nucleons seems to be reasonable for intermediate bombarding energies. The energy spectra of observed particles may be described by emission from a single moving source, as in higher energy collisions. The temperatures of the sources vary smoothly with bombarding energy, indicating that the transition to mechanisms typical of relativistic energy reactions is a smooth one. Although this smooth behavior seems to rule out any abrupt transitions such as a phase transition from a nuclear liquid to a nuclear gas, the small sizes of the systems created could cause large fluctuations, masking the sharp changes in temperature or fragment sizes typical of such transitions.

Comparison of data with the fireball model, which assumes clean cuts in the projectile and target, shows that the simple geometrical picture is inadequate at these bombarding energies, where the reaction is slow enough to allow exchange of particles between the participants and the spectators. The detailed time evolution of the thermalized subsystem remains to be determined. The system may start out as a hot spot in the target nucleus and grow into the surrounding target matter, or it may undergo a rapid explosion into nucleons and nuclear fragments. Experiments investigating the correlations among such fragments are necessary to address this question.

Midrapidity fragments with $A>4$ are emitted from similar sources. Their energy spectra and angular distributions are consistent with their formation via coalescence of nucleons emitted close together in momentum space. This agreement suggests that they arise from collisions with rather large interaction regions, and therefore small impact parameters. It remains to be determined whether one can use the emission of such fragments as an impact parameter trigger, and whether the central collisions result in a multifragmentation of the system, or in a very hot gas of nucleons which freezes out into small and large fragments.

The production of heavy fragments can also be used to learn about the entropy generated in the collision as the entropy cannot be reliably inferred from the deuteron-to-proton ratio alone. The entropy from target-like fragments is independent of the projectile identity and energy, suggesting that the target absorbs a limited amount of energy and breaks up in a similar manner regardless of the fate of the participant region. The entropy extracted from midrapidity fragments is higher, in agreement with the expectation that they arise from a more violent interaction.

Detailed dynamical descriptions of reactions in this energy regime were found to need elements of low energy reactions (such as the influence of a nuclear mean field and Pauli blocking) and of high energy reactions (the two-body dissipation mechanism inherent in nucleon-nucleon collisions). The assumption of a very short mean free path in this energy regime was found to be inadequate, especially for collisions at incident energies below 50 MeV/nucleon. It remains to be investigated at which point the low energy effects become negligible. It is unlikely that a simple cutoff in bombarding energy will be found. It is more likely that complete theories to describe the intermediate energy regime will merge with theories used for relativistic collisions, yielding similar results at the higher bombarding energies.

Coincidence experiments should help to more fully describe the bombarding energy evolution in the reaction dynamics. The further study of intermediate energy heavy ion reactions promises to allow us to form a unified picture of the response of nuclear matter from very gentle to very energetic excitation.

This work was supported by the National Science Foundation under Grant No. PHY-83-12245.

---

[*] Present address: Los Alamos National Laboratory, Los Alamos, NM 87545.

[†] Present address: Siemens, Chicago, IL.

[‡] Present address: University of Frankfurt, Frankfurt, Federal Republic of Germany.

[1] A. S. Goldhaber and H. H. Heckman, Annu. Rev. Nucl. Sci. **28**, 161 (1979).

[2] Proceedings of the International Conference on Nucleus-Nucleus Collisions [Nucl. Phys. **A400** (1983)].

[3] Proceedings of the 6th High Energy Heavy Ion Study and 2nd Workshop on Anomalons, Lawrence Berkeley Laboratory Report LBL-16281, CONF- 830675, Berkeley, December, 1983.

[4] S. Nagamiya and M. Gyulassy, Adv. Nucl. Phys. **13**, 201 (1984).

[5] J. Gosset, H. H. Gutbrod, W. G. Meyer, A. M. Poskanzer, A. Sandoval, R. Stock, and G. D. Westfall, Phys. Rev. C **16**, 629 (1977).

[6] A. Sandoval, H. H. Gutbrod, W. G. Meyer, R. Stock, Ch. Lukner, N. Van Sen, A. M. Poskanzer, J. Cosset, J.-C. Jourdain, C. H. King, G. King, G. D. Westfall, and K. L. Wolf, Phys. Rev. C **21**, 1321 (1980).

[7] S. Nagamiya, M.-C. Lemaire, E. Moeller, S. Schnetzer, G. Shapiro, H. Steiner, and I. Tanihata, Phys. Rev. C **24**, 971 (1981).

[8] R. A. Cecil, B. D. Anderson, A. R. Baldwin, R. Madey, W. Schimmerling, J. W. Kast, and D. Ortendahl, Phys. Rev. C **24**, 2013 (1981).

[9] T. J. M. Symons, P. Doll, M. Bini, D. L. Hendrie, J. Mahoney, G. Mantzouranis, D. K. Scott, K. Van Bibber, Y. P. Viyogi, H. H. Wieman, and C. K. Gelbke, Phys. Lett. **94B**, 131 (1980).

[10] T. C. Awes, G. Poggi, S. Saini, C. K. Gelbke, R. Legrain, and G. D. Westfall, Phys. Lett. **103B**, 417 (1981).

[11] B. Jakobsson, L. Carlén, P. Kristiansson, J. Krumlinde, A. Oskarsson, I. Otterlund, B. Schrøder, H.-Å. Gustafsson, T. Johansson, H. Ryde, G. Tibell, J. P. Bondorf, G. Fài, A. O. T. Karvinen, O. B. Nielsen, M. Buenerd, J. Cole, D. Lebrun, J. M. Loiseaux, P. Martin, R. Ost, P. de Saintignon, C. Guet, E. Monnand, J. Mougey, H. Nifenecker, P. Perrin, J. Pinston, C. Ristori, and F. Schussler, Phys. Lett. **102B**, 121 (1981).

[12] J. B. Natowitz, M. N. Namboodiri, L. Adler, R. P. Schmitt: R. L. Watson, S. Simon, M. Berlanger, and R. Choudhury, Phys. Rev. Lett. **47**, 1114 (1981).

[13] T. C. Awes, S. Saini, G. Poggi, C. K. Gelbke, D. Cha, R. Legrain, and G. D. Westfall, Phys. Rev. C **25**, 2361 (1982).

[14] G. D. Westfall, B. V. Jacak, N. Anantaraman, M. W. Curtin, G. M. Crawley, C. K. Gelbke, B. Hasselquist, W. G. Lynch, D. K. Scott, M. B. Tsang, M. J. Murphy, T. J. M. Symons, R. Legrain, and T. J. Majors, Phys. Lett. **116B**, 118 (1982).

[15] R. L. Auble, J. B. Ball, F. E. Bertrand, C. B. Fulmer, D. C. Hensley, I. Y. Lee, R. L. Robinson, P. H. Stelson, D. L. Hendrie, H. D. Holmgren, J. D. Silk, and H. Breuer, Phys. Rev. Lett. **49**, 441 (1982).

[16] U. Lynen, H. Ho, W. Kuhn, D. Pelte, U. Winkler, W. F. J. Müller, Y.-T. Chu, P. Doll, A. Gobbi, K. Hildenbrand, A. Olmi, H. Sann, H. Stelzer, R. Bock, H. Lohner, R. Glasow, and R. Santo, Nucl. Phys. **A387**, 129c (1982).

[17] R. Glasow, G. Gaul, B. Ludewigt, R. Santo, H. Ho, W. Kuhn, U. Lynen, and W. F. J. Müller, Phys. Lett. **108B**, 15 (1982); **120B**, 71 (1983).

[18] R. L. Auble, J. B. Ball, F. E. Bertrand, C. B. Fulmer, D. C. Hensley, I. Y. Lee, R. L. Robinson, P. H. Stelson, C. Y. Wong, D. L. Hendrie, H. D. Holmgren, and J. D. Silk, Phys. Rev. C **28**, 1552 (1983).

[19] G. D. Westfall, Z. M. Koenig, B. V. Jacak, L. H. Harwood, G. M. Crawley, M. W. Curtin, C. K. Gelbke, B. Hasselquist, W. G. Lynch, A. D. Panagiotou, D. K. Scott, H. Stöcker, and M. B. Tsang, Phys. Rev. C **29**, 861 (1984).

[20] H. Kruse, B. V. Jacak, J. J. Molitoris, G. D. Westfall, and H. Stöcker, Phys. Rev. C **31**, 1770 (1985).

[21] A. I. Warwick, H. H. Wieman, H. H. Gutbrod, M. R. Maier, J. Peter, H. G. Ritter, H. Stelzer, F. Weik, M. Freedman, D. J. Henderson, S. B. Kaufman, E. P. Steinberg, and B. D. Wilkins, Phys. Rev. C **27**, 1083 (1983).

[22] B. V. Jacak, G. D. Westfall, C. K. Gelbke, L. H. Harwood, W. G. Lynch, D. K. Scott, H. Stöcker, M. B. Tsang, and T. J. M. Symons, Phys. Rev. Lett. **51**, 1846 (1983).

[23] G. D. Westfall, J. Gosset, P. J. Johansen, A. M. Poskanzer, W. G. Meyer, H. H. Gutbrod, A. Sandoval, and R. Stock, Phys. Rev. Lett. **37**, 667 (1976).

[24] N. Stelte and R. Weiner, Phys. Lett. **103B**, 275 (1981).

[25] W. A. Friedman and W. G. Lynch, Phys. Rev. C **28**, 16 (1983).

[26] D. J. Fields, W. G. Lynch, C. B. Chitwood, C. K. Gelbke, M. B. Tsang, H. Utsunomiya, and J. Aichelin, Phys. Rev. C **30**, 1912 (1984).

[27] J. R. Wu, C. C. Chang, and H. D. Holmgren, Phys. Rev. C **19**, 370 (1979).

[28] J. R. Wu, C. C. Chang, and H. D. Holmgren, Phys. Rev. C **19**, 659 (1979).

[29] M. Bini, C. K. Gelbke, D. K. Scott, T. J. M. Symons, P. Doll, D. L. Hendrie, J. L. Laville, M. C. Mermaz, C. Olmer, K. Van Bibber, and H. H. Wieman, Phys. Rev. C **22**, 1945 (1980).

[30] G. Caskey, A. Galonsky, B. Remington, M. B. Tsang, C. K. Gelbke, A. Kiss, F. Deak, Z. Seres, J. J. Kolata, J. Hinnefeld, and J. Kasagi, Phys. Rev. C **31**, 1597 (1985).

[31] P. L. Gonthier, H. Ho, M. N. Namboodiri, J. B. Natowitz, L. Adler, S. Simon, K. Hagel, S. Kniffen, and A. Khodai, Nucl. Phys. **A411**, 284 (1983).

[32] Z. M. Koenig, Ph.D. thesis, Michigan State University, 1985 (unpublished).

[33] B. Hasselquist, G. M. Crawley, L. H. Harwood, B. V. Jacak, Z. M. Koenig, G. D. Westfall, J. E. Yurkon, R. S. Tickle, J. P. Dufour, and T. J. M. Symons, Phys. Rev. C **32**, 145 (1985).

[34] H. Stocker, R. Y. Cusson, J. A. Maruhn, and W. Greiner, Z. Phys. A **294**, 125 (1980).

[35] C. Gregoire, B. Remaud, F. Scheuter, and F. Sebille, Nucl. Phys. **A436**, 365 (1985).

[36] H. W. Bertini, R. T. Santoro, and D. W. Hermann, Phys. Rev. C **14**, 590 (1976).

[37] Y. Yariv and Z. Fraenkel, Phys. Rev. C **20**, 2227 (1979).

[38] Y. Yariv and Z. Fraenkel, Phys. Rev. C **24**, 488 (1981).

[39] J. Cugnon, T. Mizutani, and J. Vandermeulen, Nucl. Phys. **A352**, 505 (1981).

[40] J. Cugnon, D. Kinet, and J. Vandermeulen, Nucl. Phys. **A379**, 553 (1982).

[41] J. Cugnon, Nucl. Phys. **A387**, 191c (1982).

[42] V. D. Toneev and K. K. Gudima, Nucl. Phys. **A400**, 173c (1983).

[43] G. Bertsch, H. Kruse, and S. DasGupta, Phys. Rev. C **29**, 673 (1984).

[44] Rudi Malfliet, Nucl. Phys. **A420**, 621 (1984).

[45] H. Kruse, B. V. Jacak, and H. Stocker, Phys. Rev. Lett. **54**, 289 (1985).

[46] H. H. Gutbrod, A. Sandoval, P. J. Johansen, A. M. Poskanzer, J. Gosset, W. G. Meyer, G. D. Westfall, and R. Stock, Phys. Rev. Lett. **37**, 667 (1976).

[47] H. Stöcker, J. A. Maruhn, and W. Greiner, Z. Phys. A **293**, 173 (1979).

[48] H. Stöcker, J. A. Maruhn, and W. Greiner, Phys. Rev. Lett. **44**, 725 (1980).

[49] R. H. Pehl, F. S. Goulding, D. A. Landis, and M. Lenzlinger, Nucl. Instrum. Methods **59**, 45 (1968).

[50] D. F. Measday and C. Richard-Serre, Nucl. Instrum. Methods **76**, 45 (1969).

[51] F. S. Goulding and B. G. Harvey, Annu. Rev. Nucl. Sci. **25**, 167 (1975).

[52] L. D. Landau and E. M. Lifshitz, *Statistical Physics* (Addison-Wesley, New York, 1969) p. 109.

[53] M. Abramowitz and I. A. Stegun, *Handbook of Mathematical Functions* (Dover, New York, 1972).

[54] J. Gosset, J. I. Kapusta, and G. D. Westfall, Phys. Rev. C **18**, 844 (1978).

[55] A. Z. Mekjian, Phys. Rev. C **17**, 1051 (1978).

[56] A. Z. Mekjian, Phys. Rev. Lett. **38**, 640 (1977).

[57] G. F. Bertsch and J. Cugnon, Phys. Rev. C **24**, 2514 (1981).

[58] D. H. Boal and J. H. Reid, Phys. Rev. C **29**, 973 (1984).

[59] D. H. Boal, Phys. Rev. C **28**, 2568 (1983).

[60] M. C. Lemaire, S. Nagamiya, S. Schnetzer, H. Steiner, and I. Tanihata, Phys. Lett. **85B**, 38 (1979).

[61] T. C. Awes, G. Poggi, C. K. Gelbke, B. B. Back, B. G. Glago-

la, H. Breuer, and V. E. Viola, Jr., Phys. Rev. C **24**, 89 (1981).

[62]B. V. Jacak, D. Fox, and G. D. Westfall, Phys. Rev. C **31**, 704 (1985).

[63]H. A. Gustafsson, H. H. Gutbrod, B. Kolb, H. Löhner, B. Ludewigt, A. M. Poskanzer, T. Renner, H. Riedesel, H. G. Ritter, A. Warwick, F. Weik, and H. Wieman, Phys. Rev. Lett. **53**, 544 (1984).

[64]W. G. Lynch, C. B. Chitwood, M. B. Tsang, D. J. Fields, D. R. Klesch, C. K. Gelbke, G. R. Young, T. C. Awes, R. L. Ferguson, F. E. Obenstein, F. Plasil, R. L. Robinson, and A. D. Panagiotou, Phys. Rev. Lett. **51**, 1850 (1983).

[65]D. Beavis, S. Y. Fung, W. Gorn, A. Huie, D. Keane, J. J. Lu, R. T. Poe, B. C. Shen, and G. VanDalen, Phys. Rev. C **27**, 910 (1983).

[66]H. Stöcker, R. Y. Cusson, J. Maruhn, and W. Greiner, Phys. Lett. **101B**, 379 (1981).

[67]P. R. Subramanian, L. P. Csernai, H. Stöcker, J. A. Maruhn, W. Greiner, and H. Kruse, J. Phys. G **7**, L1241 (1981).

[68]H. Stöcker, J. Phys. G **10**, L111 (1984).

[69]P. J. Siemens and J. I. Kapusta, Phys. Rev. Lett. **43**, 1486 (1979).

[70]I. M. Mishustin, F. Myhrer, and P. J. Siemens, Phys. Lett. **95B**, 361 (1980).

[71]S. Nagamiya, Phys. Rev. Lett. **49**, 1383 (1982).

[72]J. Randrup and S. E. Koonin, Nucl. Phys. **A356**, 223 (1981).

[73]G. Fai and J. Randrup, Nucl. Phys. **A381**, 537 (1982).

[74]Joseph Kapusta, Phys. Rev. C **29**, 1735 (1984).

[75]J. Pochodzalla, W. A. Friedman, C. K. Gelbke, W. G. Lynch, M. Maier, D. Ardouin, H. Delagrange, H. Doubre, C. Grégoire, A. Kyanowski, W. Mittig, A. Péghaire, J. Péter, F. Saint-Laurent, Y. P. Viyogi, B. Zwieglinski, G. Bizard, F. Lefèbvres, B. Tamain, and J. Québert, Phys. Rev. Lett. **55**, 177 (1985).

[76]B. V. Jacak, H. Stöcker, and G. D. Westfall, Phys. Rev. C **29**, 1744 (1984).

[77]Ray E. L. Green and Ralph G. Korteling, Phys. Rev. C **22**, 1594 (1980).

[78]J. E. Finn, S. Agarwal, A. Bujak, J. Chuang, L. J. Gutay, A. S. Hirsch, R. W. Minich, N. T. Porile, R. P. Scharenberg, B. C. Stringfellow, and F. Turkot, Phys. Rev. Lett. **49**, 1321 (1982).

[79]C. B. Chitwood, D. J. Fields, C. K. Gelbke, W. G. Lynch, A. D. Panagiotou, M. B. Tsang, H. Utsunomiya, and W. A. Friedman, Phys. Lett. **131B**, 289 (1983).

[80]B. Jakobsson, G. Jönsson, B. Lindkvist, and A. Oskarsson, Z. Phys. A **307**, 293 (1982).

[81]G. D. Westfall, R. G. Sextro, A. M. Poskanzer, A. M. Zebelman, G. W. Butler, and E. K. Hyde, Phys. Rev. C **17**, 1368 (1978).

[82]H. H. Gutbrod, H. Löhner, A. M. Poskanzer, T. Renner, H Riedesel, H. G. Ritter, A. Warwick, F. Weik, and H. Wieman, Phys. Lett. **127B**, 317 (1983).

[83]R. Balescu, *Equilibrium and Nonequilibrium Statistical Mechanics* (Wiley, New York, 1975), p. 384.

[84]E. Uehling and G. Uhlenbeck, Phys. Rev. **43**, 552 (1933).

[85]H. H. K. Tang, C. H. Dasso, H. Esbensen, R. A. Broglia, and A. Winther, Phys. Lett. **101B**, 10 (1981).

[86]C. Y. Wong, Phys. Rev. C **25**, 1461 (1982).

[87]J. Cugnon, Phys. Rev. C **22**, 1885 (1980).

[88]G. Buchwald, L. P. Csernai, J. A. Maruhn, W. Greiner, and H. Stöcker, Phys. Rev. C **24**, 135 (1981).

[89]G. Buchwald, G. Graebner, J. Theis, J. A. Maruhn, W. Greiner, and H. Stöcker, Phys. Rev. C **28**, 1119 (1983).